Ocean Engineering 256 (2022) 111492

Contents lists available at ScienceDirect

Ocean Engineering

journal homepage: www.elsevier.com/locate/oceaneng

# A high-fidelity CFD-based model for the prediction of ship manoeuvrability in currents

Daejeong Kim *, Tahsin Tezdogan, Atilla Incecik

*Department of Naval Architecture, Ocean and Marine Engineering, University of Strathclyde, 100 Montrose Street, Glasgow, G4 0LZ, UK*

ARTICLE INFO

*Keywords:*
Computational fluid dynamics
RANS solver
Ship manoeuvrability
Current
Ship hydrodynamics
KCS

ABSTRACT

The manoeuvring behaviour of a vessel in currents differs remarkably from its behaviour in water without a current, stemming from hydrodynamic effects caused by the presence of the current. Given that vessels operating in open seas and coastal waters are mostly exposed to ocean currents, it is important to have an understanding of the influence of currents on ship manoeuvrability. In the present paper, by means of an unsteady Reynolds-Averaged Naiver-Stokes solver, a numerical study of ship manoeuvrability in different currents was performed. Firstly, a model-scale container ship (the KRISO Container Ship) was used to develop the Computational Fluid Dynamics (CFD) model capable of performing a self-propelled free manoeuvre. Then, a validation study was carried out to assess the validity of the CFD model by comparison with the available experimental results from a free-running test. Following this, a series of manoeuvring simulations (i.e., standard turning manoeuvres) in deep waters with current speed to ship speed ratios varying between −0.552 and −0.138/+0.138 and + 0.552 were conducted using the present CFD model. The numerical results demonstrated that the inclusion of the current has a remarkable influence on the turning performance of the ship, leading to significant changes in the ship trajectory and its turning parameters when compared to the inherent ship manoeuvrability in deep water without a current.

## 1. Introduction

An accurate prediction of ship manoeuvrability under realistic environmental conditions is a prerequisite for the development and use of remote-controlled ships or maritime autonomous surface ships (MASS). These ships should be capable of performing path following and collision avoidance manoeuvres within an acceptable level of safety and reliability. Given that the reliable estimation of ship manoeuvrability can be decisive for the execution of such safe autonomous operations, it is critical to accurately predict the manoeuvring performance of a ship under external disturbances (waves, winds, and currents) in which the ship is to be operated. As the prediction of ship manoeuvrability in waves have already been studied in the authors' previous research (Kim et al., 2021a, 2021b, 2021c, 2022a; Kim and Tezdogan, 2022), this study aims to comprehensively analyse the manoeuvring behaviour of a ship in different ocean currents.

Ships sailing in open seas and coastal waters are mostly exposed to ocean currents. According to the National Oceanic and Atmospheric Administration (NOAA), ocean currents (characterised by the horizontal movement of water) are generally driven by the rise and fall of the tides, wind, and thermohaline circulation (density differences in water due to temperature). It has to be highlighted that the tidal currents can travel much faster than the currents driven by wind or thermohaline circulation, indicating top daily speeds of eight knots or more in a specific sea area. For example, the Kurushima Kaikyo of the Japan inland sea can be regarded as strong tidal current waters with up to 10 knots of current (monitored by its VTS centre to ensure navigational safety). The presence of currents will lead to substantial changes in a ship's manoeuvring behaviour when compared to its inherent behaviour in calm water without current, due to the hydrodynamic effects induced by currents. In this regard, it is believed that a better understanding of ship manoeuvrability in currents may contribute to proper decision making for ship handling actions and thus safe ship operation at sea.

The estimation of the manoeuvring performance of a ship has been traditionally addressed by means of System Based (SB) methods, experimental methods, or a combination of methods. In the SB approaches, simplified mathematical models are numerically solved with the aim of carrying out manoeuvring simulations in the time domain; the

* Corresponding author.
*E-mail address:* daejeong.kim@strath.ac.uk (D. Kim).

https://doi.org/10.1016/j.oceaneng.2022.111492
Received 31 December 2021; Received in revised form 3 May 2022; Accepted 5 May 2022
Available online 21 May 2022

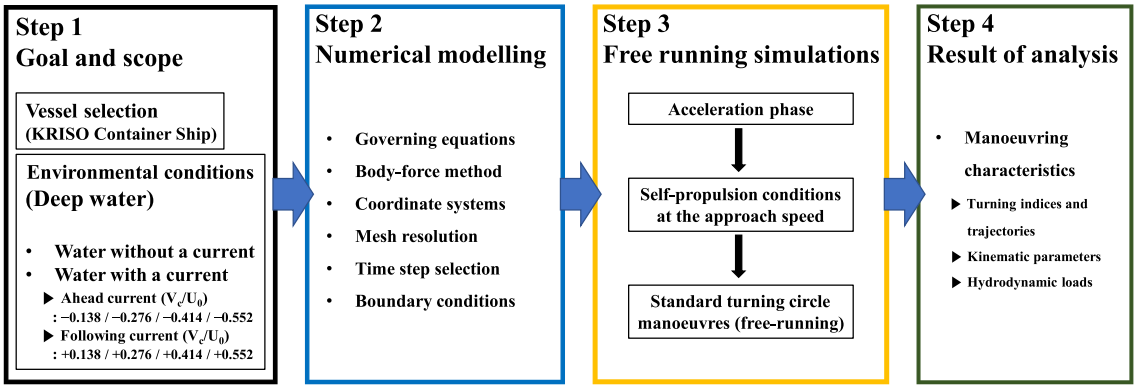


**Fig. 1.** Research methodology overview adopted in the study.

Abkowitz model (Abkowitz, 1964) and the Manoeuvring Modelling Group (MMG) model (Inoue et al., 1981; Yasukawa and Yoshimura, 2015) have been mainly adopted in this field. The accuracy of these mathematical models is strongly dependent on the validity of hydrodynamic coefficients obtained from dedicated experiments or Computational Fluid Dynamics (CFD) simulations (i.e., captive model tests), which may limit the practical applicability of the SB method. When accounting for current effects in the SB method, the surge and sway velocities in the simplified mathematical equations are simply represented by the relative velocities for current (i.e., the speed of the ship with respect to the water). In light of such limitations, it is thought that the simple use of the ship speed over water in the SB approach is not sufficient to accurately resolve the current effects occurring during ship manoeuvres. For the free-running experiment (regarded as the most reliable approach), it is highly laborious and cost-intensive to perform free-running manoeuvres as this experimental approach requires a large manoeuvring basin, manoeuvring control units, other measurement devices, and, in particular, a current generator. To the best of our knowledge, there exist no studies on free-running experiments in currents. The need to overcome these impediments identified in the SB and experimental approaches has encouraged the development of a cost-effective and high-fidelity method for the evaluation of ship manoeuvrability.

Continued computational advances have enabled CFD to increasingly gain popularity as a universal tool applicable to ship hydrodynamic problems. In the framework of CFD codes, the numerical prediction of ship manoeuvrability is made by using unsteady Reynolds-Averaged Navier-Stokes (URANS) computations coupled with the equations of rigid body motion with full six degrees of freedom. It has to be stressed that CFD-based techniques have the capability to take into account viscous effects as well as resolve complicated mutual interactions between the hull, propeller, and rudder during manoeuvres. In addition, CFD methods are advantageous in that they can provide very detailed hydrodynamic results with respect to ship manoeuvres that would be very difficult to measure experimentally. These benefits of CFD simulations have attracted great attention from academic and industrial fields in recent years, being referred to as high-fidelity simulations. In one of the first studies focusing on CFD applications to free-running ship manoeuvres, Broglia et al. (2013) carried out free-running CFD simulations to deeply investigate the turning capability of a twin-screw single-rudder model in deep calm water. In their study, a dynamic overlapping grid method was implemented to handle complex geometries and multiple bodies in relative motion, whilst the rotating propeller effects were modelled based on the actuator disk concept. Then, Mofidi and Carrica (2014) performed free-running zigzag manoeuvres in deep calm water for the fully appended geometry, eliminating the modelling of a rotating propeller to take into account all physics involved in the manoeuvre (utilising CFDShip-Iowa, which is a piece of general-purpose CFD software developed at the University of Iowa). The numerical results obtained from their study consisting of kinematic and dynamic parameters during the manoeuvre were validated against the available measured data, concluding that using CFD to compute standard manoeuvres with moving propeller and rudder is highly feasible. Similar free-running CFD simulations in deep calm water can be found in Broglia et al. (2015); Shen et al. (2015); Dubbioso et al. (2016); Wang et al. (2016); Hasanvand and Hajivand (2019); Hasanvand et al. (2021); Kim et al. (2021d). In Carrica et al. (2016) and Kim et al. (2022b), the manoeuvring performance of the KCS model in shallow calm water was analysed by a similar approach with the direct discretisation of the tank bottom.

With the increasing importance of ship manoeuvrability in waves (IMO, 2014; ITTC, 2017, 2021b), CFD free-running manoeuvres have been broadened out by the inclusion of the Stokes wave models to keep with this trend. As confirmed by extensive CFD simulations carried out on single or twin-screw vessels (including the KCS model adopted in the present paper and the ONR Tumblehome ship; Wang et al. (2017); Wang and Wan (2018); Wang et al. (2018); Kim et al. (2021a); Kim et al. (2021b); Kim et al. (2021c); Kim et al. (2022a); Kim and Tezdogan (2022)), it was revealed that waves, i.e., the presence of an external disturbance, can cause remarkable changes in a ship's manoeuvrability when compared to the inherent manoeuvrability in calm water.

Although numerous attempts have been made to investigate the manoeuvring behaviour of a ship in calm water and waves, there has been a notable lack of research into the effect of currents on ship manoeuvrability. It has been observed in real operations that vessels experience currents of different velocities and directions depending on the area the ship is to be navigated through. The importance of potential current effects and the lack of previous studies support the main argument of this paper: the analysis of the relationship between ocean currents and ship manoeuvrability is necessary. In this context, this paper was motivated to investigate the impact of currents on the manoeuvring capability of the well-known benchmarking KCS which has been widely used in the fields of ship hydrodynamics. In this study, all manoeuvring

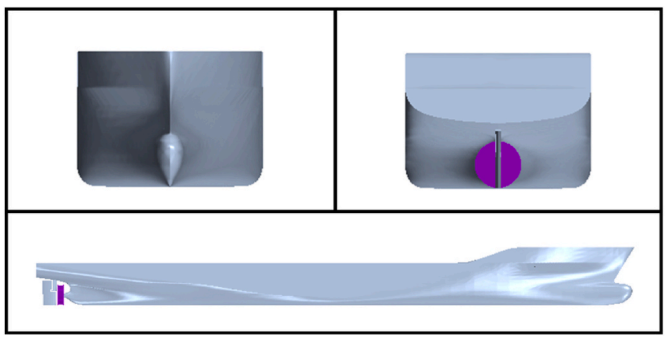

**Fig. 2.** KCS geometry with a semi balanced rudder and an actuator disk.

**Table 1**
The main particulars of the KCS model used in this work.

| Main particulars | Symbols | Model scale (1:75.24) | Full scale |
|---|---|---|---|
| Length between the perpendiculars | $L_{BP}$(m) | 3.057 | 230.0 |
| Length of waterline | $L_{WL}$(m) | 3.0901 | 232.5 |
| Beam at waterline | $B_{WL}$(m) | 0.4280 | 32.2 |
| Draft | D (m) | 0.1435 | 10.8 |
| Displacement | $\Delta(m^3)$ | 0.1222 | 52030 |
| Block coefficient | $C_B$ | 0.651 | 0.651 |
| Ship wetted area without rudder | S ($m^2$) | 1.6834 | 9530 |
| Longitudinal centre of buoyancy | % $L_{BP}$, fwd+ | −1.48 | −1.48 |
| Metacentric height | GM (m) | 0.008 | 0.6 |
| Radius of gyration | $K_{xx}/B$ | 0.49 | 0.49 |
| Radius of gyration | $K_{yy}/L_{BP}$, $K_{zz}/L_{BP}$ | 0.25 | 0.25 |
| Propeller diameter | $D_P$(m) | 0.105 | 7.9 |
| Propeller rotation direction (view from stern) | | Right hand side | Right hand side |
| Rudder turn rate | (deg/s) | 20.1 | 2.32 |

analyses were performed by means of URANS simulations.

In the present work, the turning capability of a container ship was investigated with a complete analysis of the turning indices and hydrodynamic loads experienced by the manoeuvring ship in different current conditions to obtain a deeper insight into the ship manoeuvrability. It will be shown that the numerical results can confirm the critical contribution of current effects on the manoeuvring performance of the ship in terms of the ship advance, transfer, and tactical diameter. It is believed that this study will provide a clear and detailed description of ship manoeuvrability in ocean currents and may give a significant contribution to navigational safety at sea.

This paper is organised as follows: a detailed presentation of the research methodology of the free-running CFD simulation is explained in Section 2, while its application to the manoeuvring simulations (turning circle manoeuvres) and the obtained CFD results are illustrated in Section 3. Finally, concluding remarks and future considerations wrap up the paper in Section 4.

## 2. Methodology

In this section, the research methodology adopted in this paper will be presented, with the detailed explanation provided in the contained sub-sections. The research procedure aimed at investigating the manoeuvring performance of the ship is overviewed in Fig. 1, which mainly consists of four steps: *1) goal and scope, 2) numerical modelling, 3) free running simulations, and 4) result of analysis*. As the first step, this paper formulated the research goal and objectives and defined the research scope in such a way that the effects of ocean currents on ship manoeuvrability could be identified. The second step of numerical modelling was designed to implement the numerical methods for the development of the free-running CFD model in deep water with or without a current, composed of governing equations, mesh resolution, boundary conditions, etc. In the third step, the procedures for performing free-running manoeuvres were described consisting of acceleration phases, self-propulsion conditions, and turning circle manoeuvres. The fourth step deals with the numerical results obtained from the simulations with particular attention to turning indices and trajectories, kinematic parameters, and hydrodynamic loads experienced by the manoeuvring ship. The details of each step will be shown in the following sub-sections (2.1–2.4).

### 2.1. Step 1: goal and scope

The main goal of this study is to contribute to enhancing safe ship operation at sea by obtaining a deeper insight into the effects of ocean currents on the manoeuvring capability of the ship. The specific objectives of the present paper are as follows: (1) to develop the free-running CFD model in deep waters with or without a current (2) to perform free-running CFD simulations for the selected test cases in which different conditions of ocean currents will be applied (3) to validate the numerical results obtained with the applied methodology, against the available experimental data with an aim to prove the reliability of the CFD model (4) to analyse the current effects on the manoeuvring behaviour of the ship with particular emphasis on the turning capability.

The container ship studied for the numerical simulations is the KRISO Container Ship (KCS) model with a scale factor of 75.24. The overview of the ship geometry characterised by a traditional single rudder/single propeller configuration is depicted in Fig. 2, and the

**Table 2**
The simulation cases to which the CFD model is applied.

| Case | Model scale (1:75.24) | | | | |
|---|---|---|---|---|---|
| | Approach speed $U_0$ (m/s) | Current speed $V_c$ (m/s) | $\frac{\text{Current speed}}{\text{Ship speed}}$ ($V_c/U_0$) | Froude number (Fr) | Reynolds number(Re) |
| 0 | 0.860 | 0.0000 (without a current) | 0.000 | 0.157 | $2.07 \times 10^6$ |
| 1 | 0.860 | −0.1186 (ahead current) | −0.138 | 0.157 | $2.07 \times 10^6$ |
| 2 | 0.860 | −0.2372 (ahead current) | −0.276 | 0.157 | $2.07 \times 10^6$ |
| 3 | 0.860 | −0.3558 (ahead current) | −0.414 | 0.157 | $2.07 \times 10^6$ |
| 4 | 0.860 | −0.4745 (ahead current) | −0.552 | 0.157 | $2.07 \times 10^6$ |
| 5 | 0.860 | +0.1186 (following current) | +0.138 | 0.157 | $2.07 \times 10^6$ |
| 6 | 0.860 | +0.2372 (following current) | +0.276 | 0.157 | $2.07 \times 10^6$ |
| 7 | 0.860 | +0.3558 (following current) | +0.414 | 0.157 | $2.07 \times 10^6$ |
| 8 | 0.860 | +0.4745 (following current) | +0.552 | 0.157 | $2.07 \times 10^6$ |
| Full scale | | | | | |
| Case | Approach speed $U_0$ (m/s) | Current speed $V_c$ (m/s) | $\frac{\text{Current speed}}{\text{Ship speed}}$ ($V_c/U_0$) | Froude number (Fr) | Reynolds number (Re) |
| 0 | 7.460 | 0.0000 (without a current) | 0.000 | 0.157 | $1.35 \times 10^9$ |
| 1 | 7.460 | −1.0289 (ahead current) | −0.138 | 0.157 | $1.35 \times 10^9$ |
| 2 | 7.460 | −2.0578 (ahead current) | −0.276 | 0.157 | $1.35 \times 10^9$ |
| 3 | 7.460 | −3.0866 (ahead current) | −0.414 | 0.157 | $1.35 \times 10^9$ |
| 4 | 7.460 | −4.1155 (ahead current) | −0.552 | 0.157 | $1.35 \times 10^9$ |
| 5 | 7.460 | +1.0289 (following current) | +0.138 | 0.157 | $1.35 \times 10^9$ |
| 6 | 7.460 | +2.0578 (following current) | +0.276 | 0.157 | $1.35 \times 10^9$ |
| 7 | 7.460 | +3.0866 (following current) | +0.414 | 0.157 | $1.35 \times 10^9$ |
| 8 | 7.460 | +4.1155 (following current) | +0.552 | 0.157 | $1.35 \times 10^9$ |

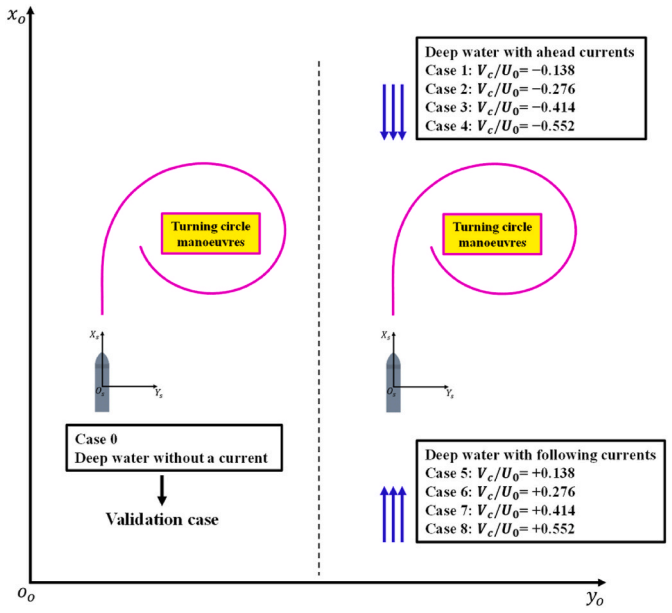


**Fig. 3.** The schematic view of the simulation cases applied to this study.

principal characteristics of the model are listed in Table 1. The present study considered nine different simulation cases for which the free-running CFD model was applied, as reported in Table 2. For the sake of clarity, the schematic representation of the cases is also depicted in Fig. 3. As a validation case for the CFD approach used in this study, a standard turning circle manoeuvre (35° starboard turn) in deep water without a current (Case 0) was performed. The experimental results of the turning circle manoeuvre produced by Hiroshima University (SIMMAN, 2020) were utilised as benchmark data for validation purposes. After the validation study, a series of numerical simulations for turning manoeuvres were carried out in different current speed to ship speed ratios (Case 1–8): 1) $V_c/U_0 = -0.138$, 2) $V_c/U_0 = -0.276$, 3) $V_c/U_0 = -0.414$, 4) $V_c/U_0 = -0.552$, 5) $V_c/U_0 = +0.138$, 6) $V_c/U_0 = +0.276$, 7) $V_c/U_0 = +0.414$, 8) $V_c/U_0 = +0.552$ (with indicating $V_c$ and $U_0$ the current speed and ship speed, respectively). A negative sign indicates ahead currents, whereas a positive sign means following currents. It can be estimated from the ratios that the currents applied in this study ranged between −8 knots and +8 knots in full scale, in correspondence to the speed of strong currents identified by NOAA. The simulation cases cover a significant range of ocean current conditions experienced by a ship in real navigation. The approach speed of the ship in all cases was chosen to be 0.86 m/s (corresponding to 14.5 knots in full scale) in a similar manner to the experiments of Hiroshima University. The corresponding Froude and Reynolds numbers were $Fr = 0.157$ and $Re = 2.07 \times 10^6$ in model scale, respectively. It has to be mentioned that all the manoeuvring analyses were conducted using deep water conditions.

### 2.2. Step 2: numerical modelling

The commercial CFD code STAR-CCM+ (version 15.04), developed by CD-Adapco, was utilised to implement the numerical simulations in this study. The detailed features of the numerical schemes adopted in this work are described in the following sub-sections.

#### 2.2.1. Governing equations

Turbulent flows around the ship were computed by the numerical solution of the unsteady Reynolds Averaged Navier-Stokes (URANS) equations, under the assumption of Newtonian, incompressible, and viscous fluid. Without considering the body forces, the continuity and momentum equations for the flow can be expressed in vectorial form as follows:

$$\nabla \cdot \boldsymbol{U} = 0 \tag{1}$$

$$\frac{\partial(\rho \boldsymbol{U})}{\partial t} + \nabla \cdot \left[\rho(\boldsymbol{U} - \boldsymbol{U}_g)\boldsymbol{U}\right] = -\nabla p + \nabla \cdot \left(\mu_{eff} \nabla \boldsymbol{U}\right) + \nabla \boldsymbol{U} \cdot \nabla \mu_{eff} + q_i \tag{2}$$

where $\nabla \cdot (\cdot)$ and $\nabla (\cdot)$ indicate the divergence and gradient operators, respectively. $\boldsymbol{U}$ is the fluid velocity and $\boldsymbol{U}_g$ is the grid velocity; p is the static pressure; ρ is the fluid density; $\mu_{eff} = \rho(\nu + \nu_t)$ stands for the effective dynamic viscosity, where $\nu$ and $\nu_t$ represent the kinematic and eddy viscosity, respectively ($\nu_t$ is obtained from the turbulence model); $q_i$ is a user-defined source term.

The Menter's Shear Stress Transport (SST) model (Menter, 1994) was adopted in this work to complete the URANS equations (for the closure of the system). The SST turbulence model is a two-equation eddy viscosity turbulence model which blends the merits of the k−ω turbulence model in the inner region of the boundary and the k-ε turbulence model in the far-field through blending functions depending on the turbulence length scale. This turbulence model has been widely adopted in the literature for free-running CFD models (Mofidi and Carrica, 2014; Carrica et al., 2016; Wang and Wan, 2018; Wang et al., 2018; Liu et al., 2020; Kim et al., 2021c). The first closure equation is the transport equation for the turbulent kinetic energy $k$, while the second one is the transport equation for the specific dissipation rate $\omega$. The two closure equations can be given as follows:

$$\frac{\partial(\rho k)}{\partial t} + \nabla \cdot (\rho k \boldsymbol{U}) = \left[\mu_t \left(\nabla \boldsymbol{U} + (\nabla \boldsymbol{U})^T - \frac{2}{3}\nabla \cdot \boldsymbol{U}\right) - \frac{2}{3}\rho k \delta_{i,j}\right] \nabla \boldsymbol{U} - \beta^* \rho \omega k + \nabla \cdot [(\mu + \sigma_k \mu_t)\nabla k] \tag{3}$$

$$\frac{\partial(\rho \omega)}{\partial t} + \nabla \cdot (\rho \omega \boldsymbol{U}) = \frac{\gamma}{\nu_t}\left[\mu_t \left(\nabla \boldsymbol{U} + (\nabla \boldsymbol{U})^T - \frac{2}{3}\nabla \cdot \boldsymbol{U}\right) - \frac{2}{3}\rho k \delta_{i,j}\right] \nabla \boldsymbol{U} - \beta \rho \omega^2 + \nabla \cdot [(\mu + \sigma_\omega \mu_t)\nabla \omega] + 2\rho(1 - F_1)\frac{\sigma_{\omega 2}}{\omega} \nabla k \cdot \nabla \omega \tag{4}$$

in which the first blending function $F_1$ is defined as $F_1 = \tanh\left\{\left[\min\left(\max\left(\frac{\sqrt{k}}{0.09\omega y}; \frac{500\upsilon}{y^2\omega}\right); \frac{4\rho\sigma_{\omega 2}k}{CD_{k\omega}y^2}\right)\right]^4\right\}$ with $CD_{k\omega} = \max\left(\frac{2\rho\sigma_{\omega 2}}{\omega}\nabla k \cdot \nabla \omega; 10^{-20}\right)$. $y$ represents the distance from the nearest wall. The eddy-viscosity coefficient in the SST model is defined as $\mu_t (= \rho\nu_t) = \frac{\rho a_1 k}{\max(a_1 \omega; \omega F_2)}$ where ω is the absolute value of the vorticity and $F_2$ is the second blending function defined by $F_2 = \tanh\left\{\left[\max\left(2\frac{\sqrt{k}}{0.09\omega y}; \frac{500\upsilon}{y^2\omega}\right)\right]^2\right\}$ The constants $\Phi$ ($\beta^*$, $\beta$, $\sigma_k$, $\sigma_\omega$, ⋯) of the turbulence model are calculated from the constants, $\Phi_1$, $\Phi_2$, as follows: $\Phi = F_1\Phi_1 + (1 - F_1)\Phi_2$. The constants of the formulas can be found in Menter (1994) for details.

The Volume of Fluid (VOF) method was adopted to model three-

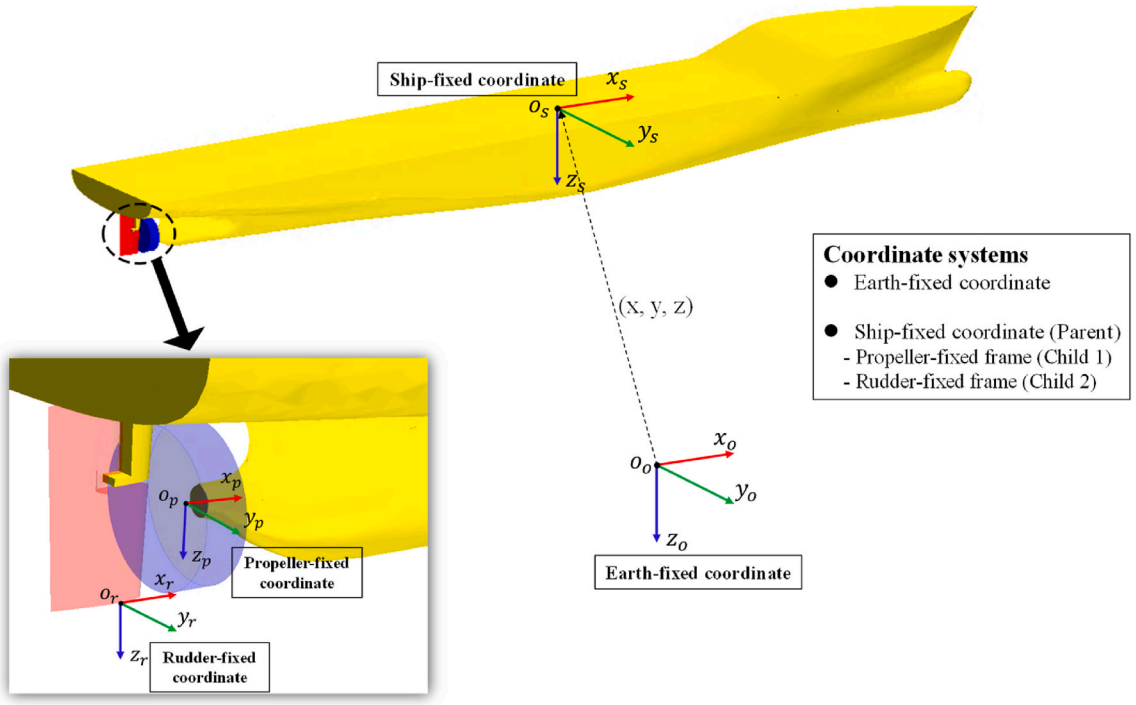


**Fig. 4.** The reference coordinate systems of the free-running simulation, adapted from Kim and Tezdogan (2022).

dimensional free-surface flows and the transport equation can be written as (Siemens, 2020):

$$\frac{\partial \alpha_i}{\partial t} + \nabla \cdot \left[\alpha_i \left(\boldsymbol{U} - \boldsymbol{U}_g\right)\right] = S_{\alpha_i} - \frac{\alpha_i}{\rho_i}\frac{D\rho_i}{Dt} - \frac{1}{\rho_i}\nabla \cdot \left(\alpha_i \rho_i \boldsymbol{v}_{d,i}\right) \tag{5}$$

where $\alpha_i$ denotes the volume fraction of phase i and its value varies from 0 to 1 to describe the relative proportion of fluid in each cell ($\alpha = 0$: non-wetting phase (air), $0 < \alpha < 1$: two-phase interface (free surface), $\alpha = 1$: wetting phase (water)). In the two-phase interface, its density and viscosity are expressed as a smooth function of the volume fraction. As the simulation evolves in time, the volume fraction function defined in the whole computational domain is advected by the underlying fluid motion. $S_{\alpha_i}$ is a user-defined source term of phase i; $\frac{D\rho_i}{Dt}$ is the Lagrangian derivative of the phase densities $\rho_i$; $\boldsymbol{v}_{d,i}$ is the diffusion velocity. As stated in Di Mascio et al. (2007), the VOF method can be advantageous in treating complex interface evolutions, even breaking and reconnecting surfaces, and in its mass conservation properties. It is worth noting that source terms for the momentum equation ($q_i$) and the VOF transport equation ($S_{\alpha_i}$) can be employed to satisfactorily reduce the accumulation errors due to undesired wave reflections occurring at domain boundaries (Perić and Abdel-Maksoud, 2018). The VOF approach has been used in many other studies performed by means of CFD simulations to position the free surface, such as Tezdogan et al. (2016), Kavli et al. (2017), Terziev et al. (2019), and Terziev et al. (2020).

The computations in this work are all based on the URANS solver which uses a finite volume method that discretises the Navier-Stokes equations. The spatial discretisation of the convection and diffusive terms of the governing transport equations was achieved through a second-order upwind scheme and a second-order centred scheme, respectively. The temporal terms in the governing equations were discretised with a second-order implicit backward Euler scheme. For pressure-velocity coupling, the SIMPLE (Semi-Implicit Method for Pressure-Linked Equations) algorithm was used with under-relaxation factors of 0.7 for velocities and 0.4 for pressure as a segregated approach.

### 2.2.2. Body-force method

An actuator disk model based on the body-force method was adopted in the present CFD model to simulate a marine propeller operating in behind-hull conditions. According to the body-force method, propeller effects can be taken into account by a field of axial and tangential body forces being distributed within an actuator disk of finite thickness. The major advantages of this approach lie in its capability in providing a reliable estimation of the flow field induced by the mutual interactions between the hull, the propeller, and the rudder, as well as in its computational efficiency. It is required to enter a number of input variables into the Star-CCM+ software for the completion of the propeller modelling, such as the open water characteristics, the geometric properties, and the rotational speed of the propeller intended to be used in the simulation. (Siemens, 2020). The axial and tangential components of the body forces over the prescribed actuator disk are given as follows:

$$f_{bx} = A_x r^* \sqrt{1 - r^*} \tag{6}$$

$$f_{b\theta} = A_\theta \frac{r^* \sqrt{1 - r^*}}{r^*(1 - r''_h) + r''_h} \tag{7}$$

$$r^* = \frac{r'' - r''_h}{1 - r''_h}, r''_h = \frac{R_H}{R_P} \text{ and } r'' = \frac{r}{R_P} \tag{8}$$

where $f_{bx}$ indicates the body force component in axial direction, $f_{b\theta}$ indicates the body force component in tangential direction, r is the radial coordinate, $R_H$ is the hub radius and $R_P$ is the propeller radius. The constants $A_x$ and $A_\theta$ are computed in the following equations, with T, Q, and $t_{disk}$ representing the thrust, the torque, and the actuator disk thickness, respectively.

$$A_x = \frac{105}{8} \cdot \frac{T}{\pi t_{disk}(3R_H + 4R_P)(R_P - R_H)} \tag{9}$$

$$A_\theta = \frac{105}{8} \cdot \frac{Q}{\pi t_{disk} R_P (3R_H + 4R_P)(R_P - R_H)} \tag{10}$$

It has to be pointed out that when computing propulsive performance, the actual velocity field around the propeller can be accounted

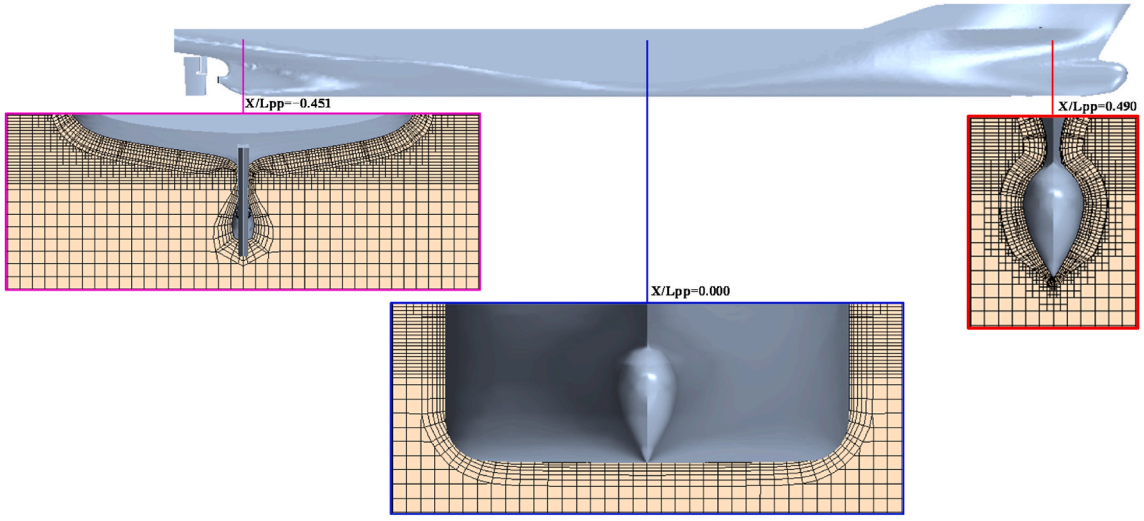


(a) Stern, midship, and bow cross-sections

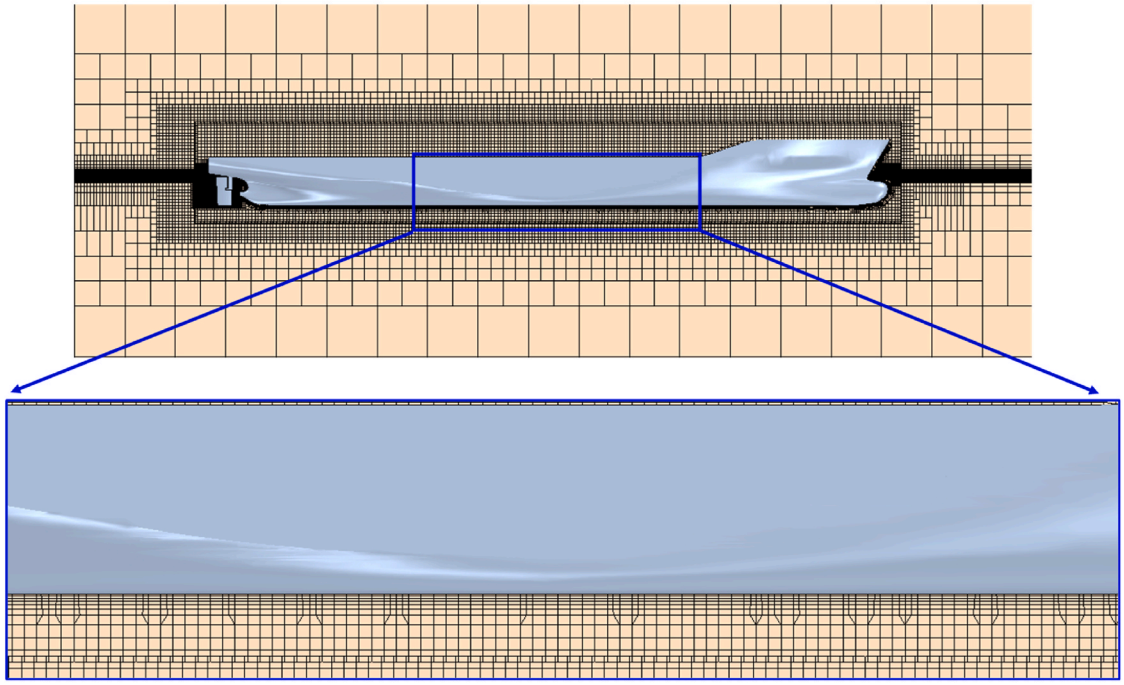

(b) Profile view cross-section of the domain

**Fig. 5.** Mesh structure of the computational domain.

for by an introduction of the volume-averaged velocity over the inflow velocity plane located upstream of the disk. As a consequence, the hull-propeller interaction can be considered during the free-running manoeuvre. The inflow velocity plane was designed to have an offset of 10% of the actuator disk diameter with respect to the actuator disk origin, and its diameter was set to be 10% larger than the diameter of the actuator disk (diameter of the plane: 0.1155 m, offset from the disk origin: 0.01 m), as recommended by Siemens (2020). In Broglia et al. (2015) and Dubbioso et al. (2016), it was reported that an actuator disk model needs to have the capability in accounting for the side forces originated by the propeller during ship manoeuvres, which could influence the prediction accuracy of manoeuvring results. However, the actuator disk model adopted in this work did not take into account the propeller side force experienced by the ship during manoeuvres. In the authors' previous studies (Kim et al., 2021c, 2022b), nonetheless, the actuator disk model for the KCS propeller has already demonstrated promising results by performing turning and zigzag manoeuvres.

### 2.2.3. Coordinate systems

Four different types of reference frames were used for the free-running CFD model as listed in the following (Fig. 4):

- Earth-fixed coordinate frame ($o_o - x_o y_o z_o$): An inertial coordinate frame with its origin fixed at point $o_o$. When the solution is initialised, the axis $o_o x_o$ is parallel to the ship's longitudinal axis (positive forward), the axis $o_o y_o$ is parallel to the ship's transverse axis (positive starboard side), and the axis $o_o z_o$ completes a right-handed orthogonal frame (positive downwards).
- Ship-fixed coordinate frame ($o_s$ - $x_s y_s z_s$): a moving reference frame fixed to the hull with the origin fixed at the centre of mass of the ship.

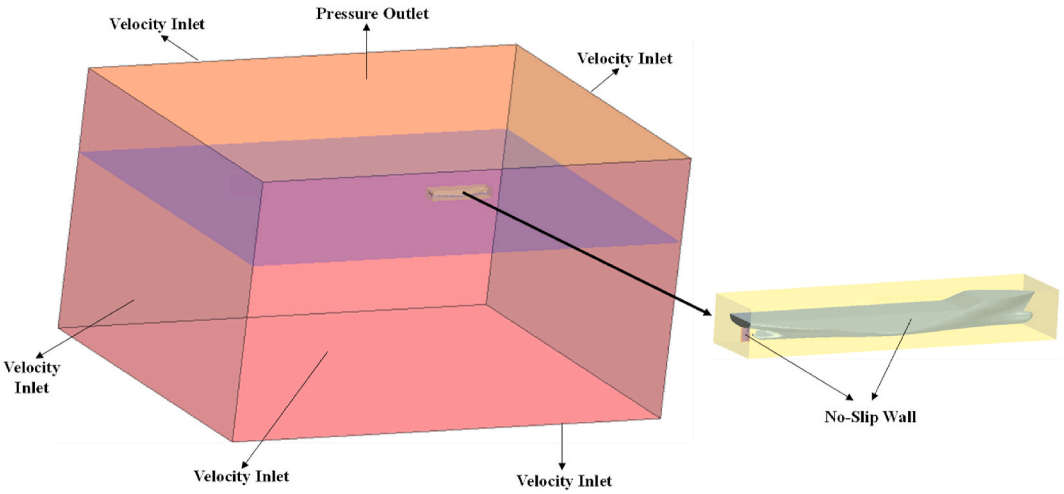


**Fig. 6.** The schematic view of the background and overset regions and the applied boundary conditions for the free-running simulations.

The axis $o_sx_s$ is aligned with the ship's longitudinal axis (directed towards the bow), the axis $o_sy_s$ is directed towards the starboard side, and the $o_sz_s$ is directed towards downward direction as a right-handed orthogonal frame.

- Propeller-fixed coordinate frame ($o_p$ - $x_py_pz_p$): a moving reference frame fixed to the hull with the origin located at the centre of the propeller. The axis $o_px_p$ indicates the direction in which thrust force is produced by the actuator disk.
- Rudder-fixed coordinate frame ($o_r$ - $x_ry_rz_r$): a moving reference frame fixed to the hull with the origin taken at the bottom of the rudder on the Aft Perpendicular (AP). The axis $o_rz_r$ is the axis about which the rudder blade rotates (the positive sign of the rudder angle: deflection to the port side).

In this study the dynamic behaviour of the ship during free-running manoeuvres was simulated with the use of the Dynamic Fluid Body Interaction (DFBI) approach (Siemens, 2020). The flow field was solved in the Earth-fixed inertial coordinate system so that the hydrodynamic forces and moments acting on the ship were computed. The forces and moments in the Earth-fixed frame were then projected into the non-inertial ship-fixed coordinate system to solve the motion equations of the rigid body which is given as follows:

$$\begin{cases} X = m[\dot{u} + qw - rv] \\ Y = m[\dot{v} + ru - pw] \\ Z = m[\dot{w} + pv - qu] \end{cases} \tag{11}$$

$$\begin{cases} K = I_{xx}\dot{p} + (I_{zz} - I_{yy})rq \\ M = I_{yy}\dot{q} + (I_{xx} - I_{zz})pr \\ N = I_{zz}\dot{r} + (I_{yy} - I_{xx})pq \end{cases} \tag{12}$$

in which m is the mass of body

u, v, w are the surge/sway/heave velocities
p, q, r are the roll/pitch/yaw angular velocities
X, Y, Z are the surge/sway/heave resultant forces acting on the ship
K, M, N are the roll/pitch/yaw resultant moments acting on the ship
$I_{xx}$, $I_{yy}$, $I_{zz}$ are the moments of inertia about the principle axes in the body frame

The velocities of the ship can be calculated by solving Equations (11) and (12) and the new position and attitude of the ship can be obtained by integrating these kinematic parameters over time.

#### 2.2.4. Mesh generation

Computational grids were generated by means of the automatic meshing facility in Star-CCM+, leading to the total number of grid cells being about 6.2 million. The volume meshes were generated by using the trimmed volume method which has the capability of providing a high-quality grid for complex mesh problems. The ensuing mesh was formed predominantly of unstructured hexahedral cells with trimmed cells adjacent to the model surface. A surface remesher on the domain, hull, and rudder surfaces was executed to ensure that the overall quality of part surfaces was sufficiently enhanced. A prism mesh model was also employed to adjust the grid spacing near the solid surfaces, such that a set of six layers of orthogonal prismatic cells next to the surfaces was generated. The use of prismatic grids can improve the accuracy with respect to the resolution of the turbulent boundary layer close to the surfaces. The present CFD model adopted the all-y+ wall treatment in STAR-CCM+ to model near-wall turbulence quantities such as wall shear stress, turbulent production, and turbulent dissipation. The local mesh refinement was implemented for the free surface region, the bow, the stern, the tight gap parts between the rudder blade and horn, and the propeller wake region with an aim to obtain more accurate flow characteristics. The final computational mesh of the CFD model is shown in Fig. 5.

In the context of free-running CFD simulations, a dynamic overlapping grid technique should be used in conjunction with the RANS solver to handle the complex motions of the CFD model. A great advantage of the "overlapping grid approach" is that it allows overset regions to move independently without any constraints while building a high-quality grid (i.e., smooth, and orthogonal) around the hull and rudder blade. A typical simulation using the overlapping grid method has a background region enclosing the entire computational domain and one or more overset regions that surround bodies such as a ship hull, propeller, or rudder. As implemented in Kim et al. (2021c), the computational domain for the present numerical model was decomposed into three different regions using the overlapping grid technique as follows: 1) background region, 2) hull overset region, and 3) rudder blade overset region. When using the overlapping technique, a hole-cutting process for coupling the overset regions with the background region is implemented. The resulting cells in the computational domain are categorised into three groups: 1) active cells, 2) inactive cells, 3) acceptor cells. The value of a flow variable $\varphi$ of the acceptor cell of one region is obtained by a weighted linear interpolation scheme from the donor cells (the active cells) in another region:

$$\varphi = \sum_{i=1}^{n} \omega_i \varphi_i \tag{13}$$

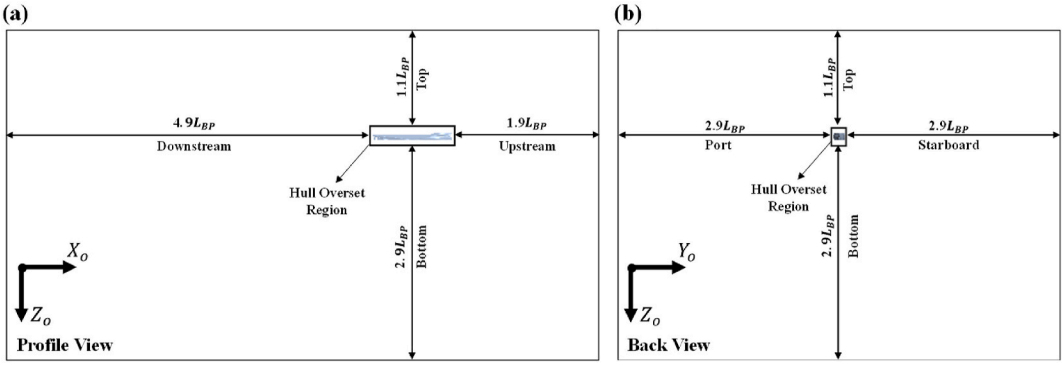


**Fig. 7.** The dimensions of the computational domain for the free-running simulations, (a) profile view of the domain, (b) back view of the domain.

in which $\omega_i$ is the interpolation weighting factor and $\varphi_i$ is the value of the dependent variable $\varphi$ at the donor cell (the subscript i runs over all the donor nodes of an interpolation element).

### 2.2.5. Determination of the time step

The time-step size of the simulations in this work was selected to be $\Delta t = 0.005$ s, ensuring the Courant-Friedrichs-Lewy (CFL) number is less than unity during the computations to avoid numerical instabilities. The chosen time step also satisfied the recommendation for the time-step condition of $\Delta t \leq 0.01L/U$ put forward by ITTC (2014), in which L and U denote ship length and ship speed, respectively. $\Delta t = 0.005$ s is even times lower than the value calculated from the recommendation by ITTC (2014). It has been already demonstrated that the use of $\Delta t = 0.005$ s is sufficiently appropriate when performing free-running simulations of the 1/75.24 scale KCS model in the authors' previous study (Kim et al., 2021c), yielding reliable numerical results.

### 2.2.6. Computational domain and boundary conditions

A general view of the background and overset regions with the notations indicating the applied boundary conditions is illustrated in Fig. 6, and the locations of the boundaries are presented in Fig. 7. As can be seen, a velocity inlet boundary condition was applied at the upstream, downstream, side, and bottom boundaries. The selection of the velocity inlet condition for these boundaries can prevent a velocity gradient from occurring between the fluid and wall. The inlet flow properties in the CFD software package are the functions of the flat wave model used to simulate the free surface, in which the velocity and direction of the flow at all inlet boundaries were represented with respect to the earth-fixed reference. In this work, the constant velocity and direction of the flow at the inlet boundaries were set to the corresponding values of the current. Hence, the constant propagation of the ocean current with a specific speed and direction could be achieved in the computational domain during the free-running simulation. A pressure outlet boundary condition was imposed at the top boundary. The ship hull and rudder blade were both selected as no-slip boundary conditions. It was observed that the presence of strong currents resulted in undesired wave reflections at the downstream and side boundaries of the domain during the computations, by moving the Kelvin wake generated by the manoeuvring ship quickly towards the walls. In order to mitigate wave reflection from the walls, the VOF wave damping capability of the software package with a damping length equal to 1.6 $L_{BP}$ (~5.0 m) was applied at the vertical boundaries. It has to be stated that in CFD applications with ship models in water with or without a current, there are no definite recommendations regarding how to define the damping length. However, several past studies (Tezdogan et al., 2015; Demirel et al., 2017; Kim et al., 2021c) using STAR-CCM+ utilised the VOF wave damping capabilities of the software with a damping length of more than 1 $L_{BP}$ to prevent reflections from the boundaries, presenting promising results. It is thought that the damping length could be determined based on a trial-and-error procedure and by repeating the simulation to avoid undesired wave reflections. It is worth mentioning that the size of the background domain generated in this work was larger than that used in the authors' previous literature (Kim et al., 2021c) due to the possible occurrence of wave reflection from the walls under strong current conditions. The remarkable difference from the domain created in the previous study to perform free-running manoeuvres in calm water without a current is that the downstream and side boundaries were located 4.9 $L_{BP}$ and 2.9 $L_{BP}$ away from the ship body, respectively, as wave reflection from the boundaries was prominent. The dimension of the domain in this study has been determined based on a trial-and-error procedure and by repeating the free-running simulation in the strongest current to mitigate wave reflections.

The motion of the background region was designed to follow the ship during the free-running manoeuvre, only translating and rotating in the horizontal plane (i.e., the surge, sway, and yaw motions of the ship). It has to be pointed out that when using a fixed background region for the simulation, the size of the background must cover the whole trajectory of the manoeuvring ship, leading to a relatively large background domain and the increase of computational time. The rudder overlapping region tailored to the rudder blade was forced to follow the ship but can have motion relative to it based on the rudder controller which will be illustrated in Section 2.3. The 6DOF motion capability was assigned to the ship overset region, such that the ship can freely move in full six degrees of freedom based on the hydrodynamic forces and moments acting on the ship.

## 2.3. Step 3: free running simulations

As presented in Section 2.1, the turning capability of the ship in different currents was investigated by performing the turning manoeuvre. The procedure of the free-running CFD simulation in this work was consistent with that generally adopted in full-scale sea trials or model-scale experiments, consisting of three phases: 1) Acceleration, 2) Self-propulsion and 3) Turning circle manoeuvre. Phase 1 is the acceleration phase in which the ship model was accelerated from the rest to the prescribed approach speed (i.e., $U_0 = 0.86$ m/s). After the target approach speed was achieved, the propeller revolution rate was kept constant for the stabilisation of self-propulsion in Phase 2. In Phase 3, the ship model started to perform the standard turning circle manoeuvre (35° starboard turns) in accordance with the control mechanism as given by the following equation:

$$\delta(t) = \max(-35, \min(0, -kt)) \tag{14}$$

in which $t$ indicating the time (s) elapsed after the start of Phase 3, $\delta(t)$ the rudder angle (°), k the maximum rudder rate ($k = 20.1°/s$).

**Step 4.** Results of analysis

In step 4, the turning performance of the ship in different current conditions was evaluated based on all the numerical results obtained

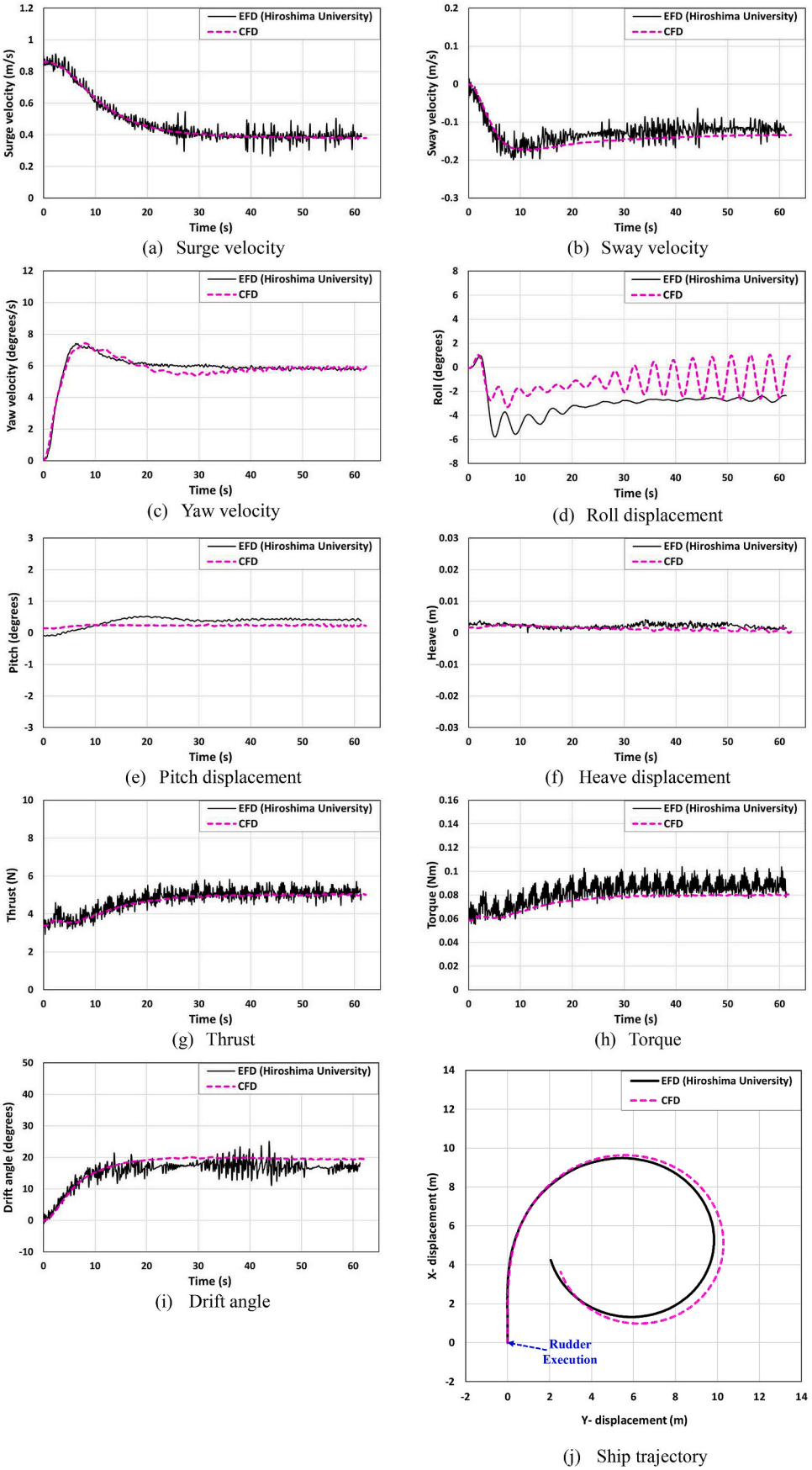


**Fig. 8.** The comparisons of the kinematic parameters, motions, propeller characteristics, drift angle, and trajectory experienced by the ship during the turning manoeuvre in deep water without a current (Case 0).

**Table 3**
The comparison of the trajectory and kinematic parameters (Case 0).

| Parameters | CFD | EFD (SIMMAN, 2020) | Error (%) |
|---|---|---|---|
| RPS at self-propulsion point | 10.56 | 10.40 | 1.58 |
| Advance (m) | 9.38 | 9.29 | 0.97 |
| Transfer (m) | 4.07 | 4.16 | −2.16 |
| Time for yaw 90° (s) | 15.46 | 15.64 | −1.15 |
| Tactical diameter (m) | 10.02 | 9.66 | 3.72 |
| Time for yaw 180° (s) | 31.12 | 30.50 | 2.03 |
| Speed loss (m/s) | 0.476 | 0.472 | 0.85 |
| Yaw velocity (degrees/s, steady phase) | 5.84 | 5.83 | 0.17 |

from this study. The main aspect of this work was dedicated to the detailed analysis of the trajectories, kinematic parameters, and hydrodynamic loads experienced by the manoeuvring ship.

## 3. Case studies (Results of Step 4)

### 3.1. Verification and validation study

Generally, the simulation numerical uncertainty can be assessed by conducting a verification study (for example, grid and time-step sensitivity studies). However, similar to most previous studies performed in the same area (Mofidi and Carrica, 2014; Wang and Wan, 2018; Wang et al., 2018; Liu et al., 2020), a verification study has not been

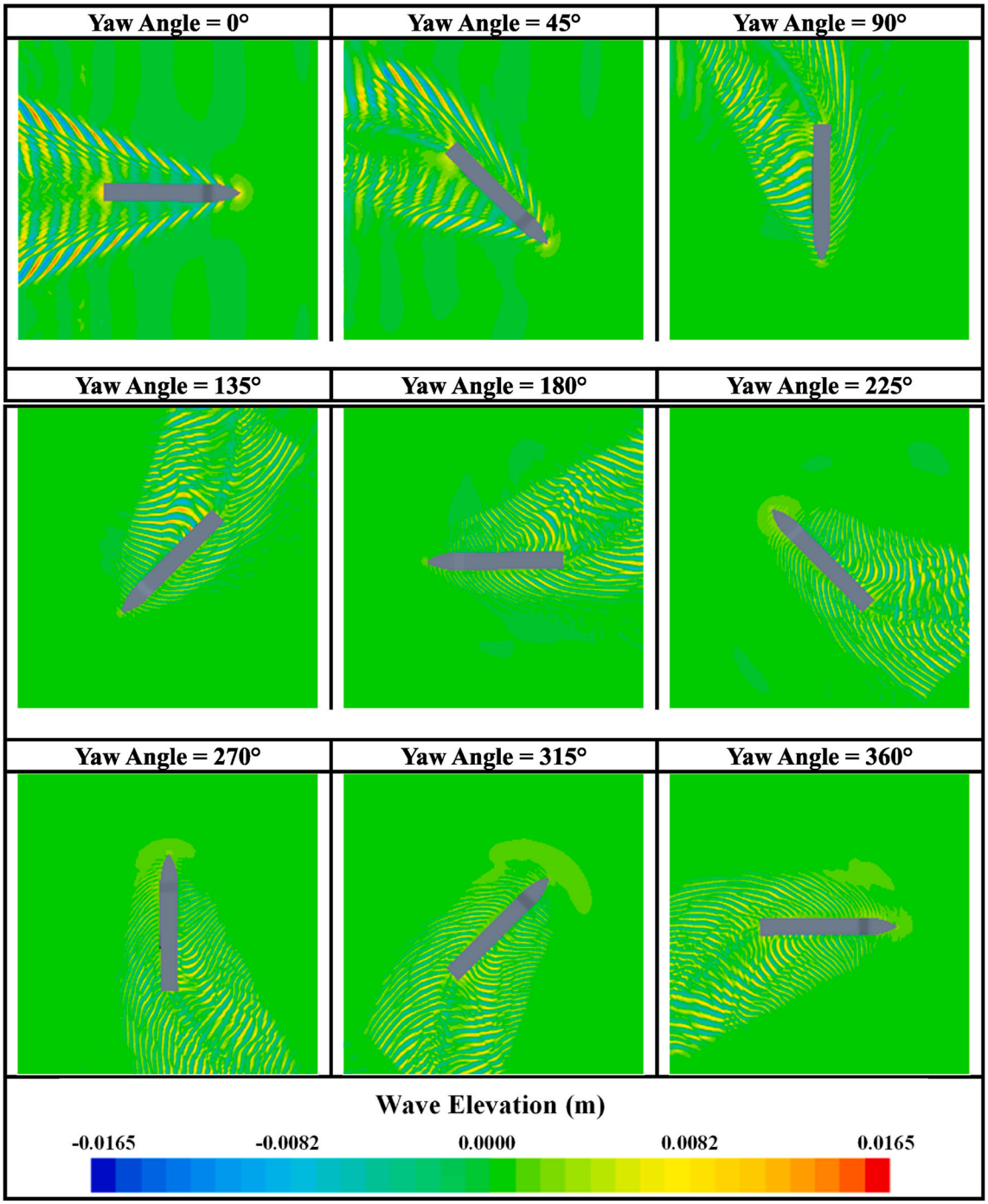


**Fig. 9.** The free surface elevation during the turning manoeuvre for Case 0.

**Table 4**
The mean value of the ship resistance and the propeller revolution rate at self-propulsion in model scale.

| | Case 0 | Case 1 | Case 2 | Case 3 | Case 4 | Case 5 | Case 6 | Case 7 | Case 8 |
|---|---|---|---|---|---|---|---|---|---|
| Ship resistance (N) | 3.35 | 4.16 | 5.19 | 6.45 | 7.87 | 2.61 | 1.99 | 1.63 | 0.99 |
| Propeller rev. (RPS) | 10.56 | 12.00 | 13.42 | 15.05 | 16.60 | 9.25 | 8.25 | 7.10 | 5.50 |

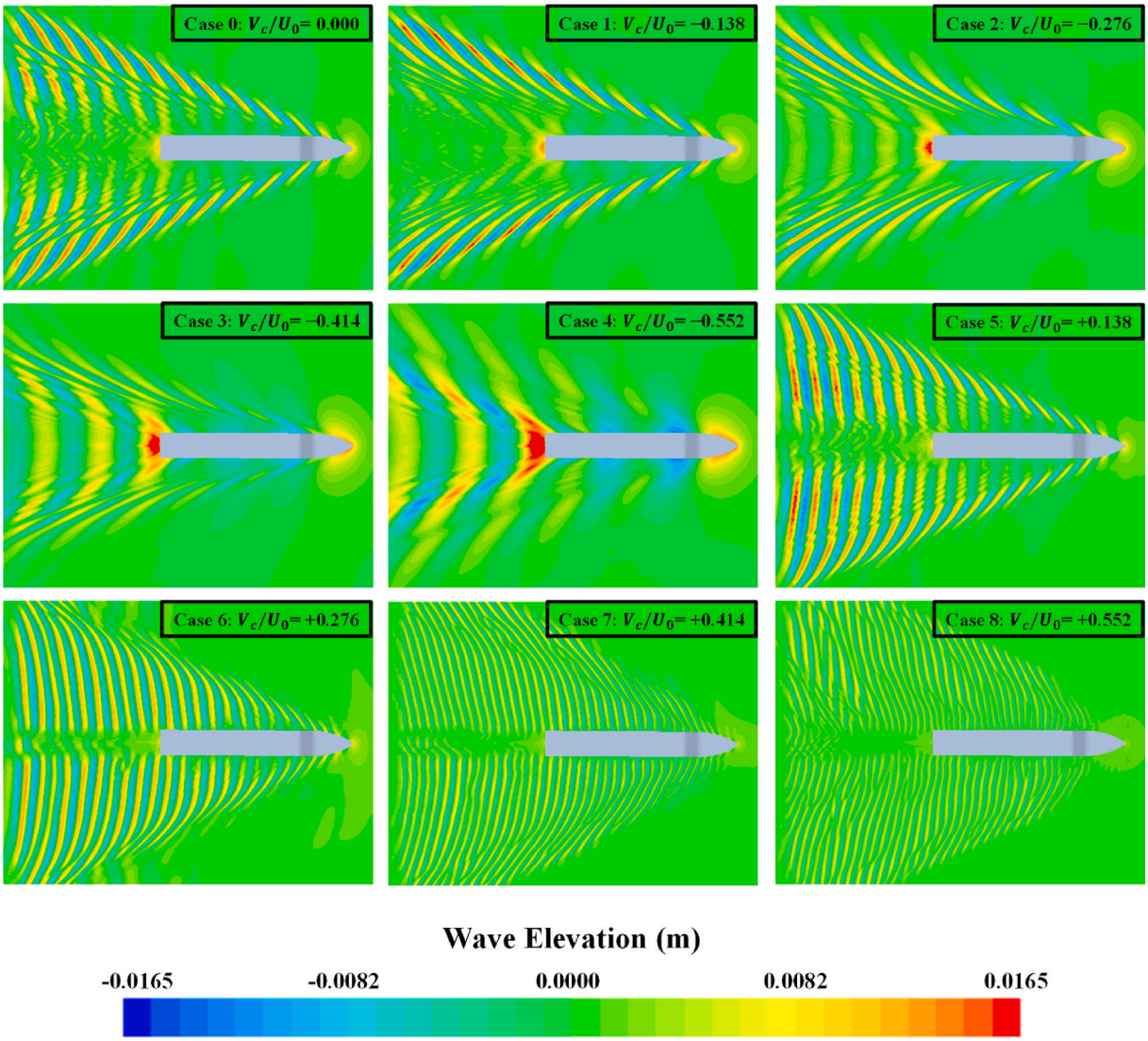


**Fig. 10.** Measured wave pattern around the advancing ship at self-propulsion (Fr = 0.157).

undertaken in this work due to not only the high computational cost of free-running CFD simulations but also the difficulty arising from refining and coarsening overset grids. Verification studies of similar problems utilising the almost same grid topology and methodology have been carried out by the authors' previous research (Kim et al., 2021c) for the free-running manoeuvre in regular waves. According to their results, the numerical uncertainties for the computation of the ship advance, transfer, and tactical diameter were reported to be a maximum of 0.28% in the grid-spacing convergence study and 0.19% in the time-step convergence study using the grid convergence index method. Monotonic convergence was attained in the uncertainty studies.

As outlined in Section 2, Case 0 (deep water without a current) was used for the validation of the present CFD model against the experiment (a free-running model test) performed by Hiroshima University (SIMMAN, 2020). It has to be pointed out that there are no available experimental results for the KCS's manoeuvrability in currents in the literature so that the validation study concerning the current conditions (Case 1–8) could not be conducted in this work. Fig. 8 presents a comparison of the time histories of the kinematic parameters, motions, propeller characteristics, drift angle, and the trajectory experienced by the ship during the turning manoeuvre in deep water without a current between this study's CFD model and the experiment. In the presented results, t = 0 is the time at which the rudder blade started to be deflected for the turning manoeuvre. The numerical simulation stopped when the ship's heading angle variation reached 360° based on the general procedure by IMO (2002). The comparison in terms of the ship's velocity in the horizontal plane consisting of the surge, sway, and yaw velocities confirmed the satisfactory agreement between CFD and Experimental Fluid Dynamics (EFD) (Fig. 8 (a)–(c)); a slight overprediction of the sway velocity was observed during the steady phase of the turn. Regarding the ship's roll motion, an error of approximately 3° was observed during the turning manoeuvre (Fig. 8 (d)). The

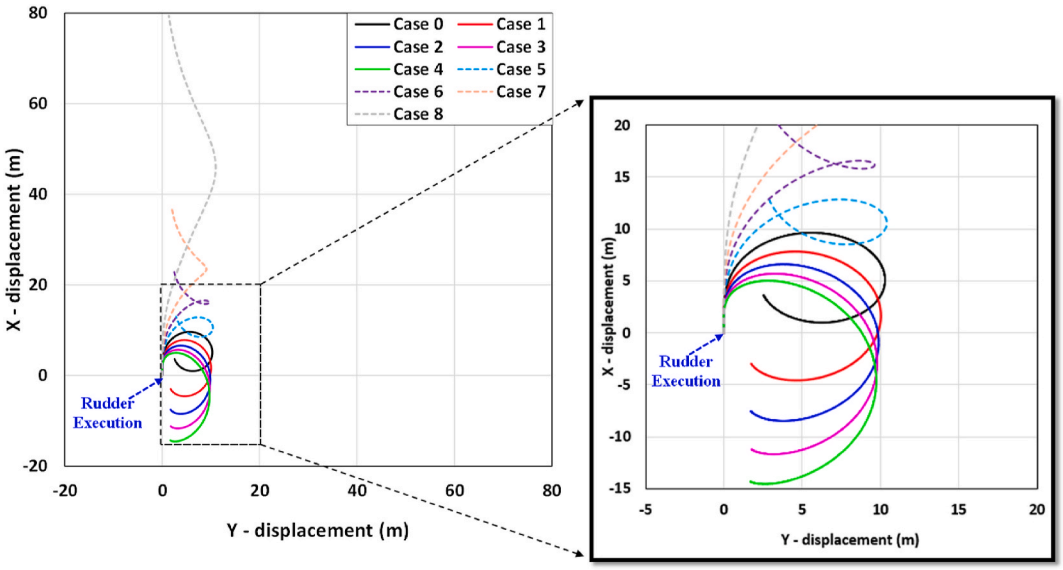


**Fig. 11.** The predicted turning trajectories for all cases.

**Table 5**
CFD results: turning parameters.

| Parameters (CFD results) | Case 0 | Case 1 | Case 2 | Case 3 | Case 4 |
|---|---|---|---|---|---|
| | Ahead current conditions | | | | |
| Advance ($m$) | 9.38 (**3.07** $L_{BP}$) | 7.81 (**2.55** $L_{BP}$) | 6.60 (**2.16** $L_{BP}$) | 5.63 (**1.84** $L_{BP}$) | 4.86 (**1.59** $L_{BP}$) |
| Transfer ($m$) | 4.07 (**1.33** $L_{BP}$) | 4.02 (**1.32** $L_{BP}$) | 4.00 (**1.31** $L_{BP}$) | 3.98 (**1.30** $L_{BP}$) | 3.96 (**1.29** $L_{BP}$) |
| Time for yaw 90° ($s$) | 15.46 | 13.58 | 12.17 | 10.99 | 10.13 |
| Tactical diameter ($m$) | 10.02 (**3.28** $L_{BP}$) | 9.78 (**3.20** $L_{BP}$) | 9.66 (**3.16** $L_{BP}$) | 9.56 (**3.13** $L_{BP}$) | 9.51 (**3.11** $L_{BP}$) |
| Time for yaw 180° ($s$) | 31.12 | 27.03 | 23.92 | 21.33 | 19.53 |
| Parameters (CFD results) | Case 5 | Case 6 | Case 7 | Case 8 | |
| | Following current conditions | | | | |
| Advance ($m$) | 11.90 (**3.89** $L_{BP}$) | 14.14 (**4.63** $L_{BP}$) | 16.90 (**5.53** $L_{BP}$) | 24.27 (**7.94** $L_{BP}$) | |
| Transfer ($m$) | 4.26 (**1.39** $L_{BP}$) | 3.95 (**1.29** $L_{BP}$) | 3.59 (**1.17** $L_{BP}$) | 3.51 (**1.15** $L_{BP}$) | |
| Time for yaw 90° ($s$) | 18.74 | 20.91 | 23.72 | 33.28 | |
| Tactical diameter ($m$) | 10.15 (**3.32** $L_{BP}$) | 9.39 (**3.07** $L_{BP}$) | 8.84 (**2.89** $L_{BP}$) | 10.46 (**3.42** $L_{BP}$) | |
| Time for yaw 180° ($s$) | 36.85 | 40.72 | 47.09 | 76.5 | |

underestimation of the roll angle can be attributed to the limitation of the present disk model that cannot take into account the side force of the propeller during the manoeuvre. As expected, only small pitch and heave motions were observed both numerically and experimentally due to the absence of external disturbances, showing a reasonable agreement between the CFD and EFD results (Fig. 8 (e) and (f)). The CFD results for the thrust and torque experienced by the ship during the manoeuvre were found in good agreement with the experimental data; the predicted trend qualitatively and quantitatively corresponded well with the experiment (Fig. 8 (g) and (h)). For the drift angle experienced by the ship performing the turning manoeuvre, an error of about 2.4° was estimated during the steady phase of the turn (Fig. 8 (i)). It can be seen that the predicted trajectory experienced by the manoeuvring ship was fairly well consistent with the experiment (Fig. 8 (j)).

In addition, Table 3 presents a comparative analysis in terms of the ship advance, transfer, tactical diameter, time to 90°/180° yaw angle change, and kinematic parameters in the steady phase of the turn. In the table, the discrepancies between the numerical and experimental results are reported as well. The free-running CFD model has shown good agreement with respect to the trajectory and kinematic parameters against the experiment. It can be seen from Table 3 that the largest error was observed for the tactical diameter; however, the error remained below 4%. In light of the acceptable agreement evidenced from Fig. 8 and Table 3, it can be claimed that the present CFD model enables the reliable estimation of the manoeuvring performance of the ship in question.

Fig. 9 displays the consecutive views of the free surface elevation around the ship performing the turning manoeuvre in deep water without a current (Case 0). As seen in the sequence of the pictures, the Kelvin wave generated by the ship was more visible during the initial phase of the turn (i.e., when the ship was turning at a relatively high forward speed). It can be also observed that the free surface was not disturbed much when the ship was manoeuvring at a relatively low forward speed (i.e., during the steady phase of the turn).

### 3.2. Self-propulsion

The self-propulsion computations were first conducted to obtain the approach speed (0.86 m/s), allowing the ship to move in full 6DOF with the moving rudder controlled by a Proportional-Integral-Derivative (PID) controller for course-keeping control before the turning manoeuvre (as described in Kim et al. (2021c)). The propeller revolution rate for each case was continuously adjusted during the acceleration phase by using a Proportional-Integral (PI) controller until the approach

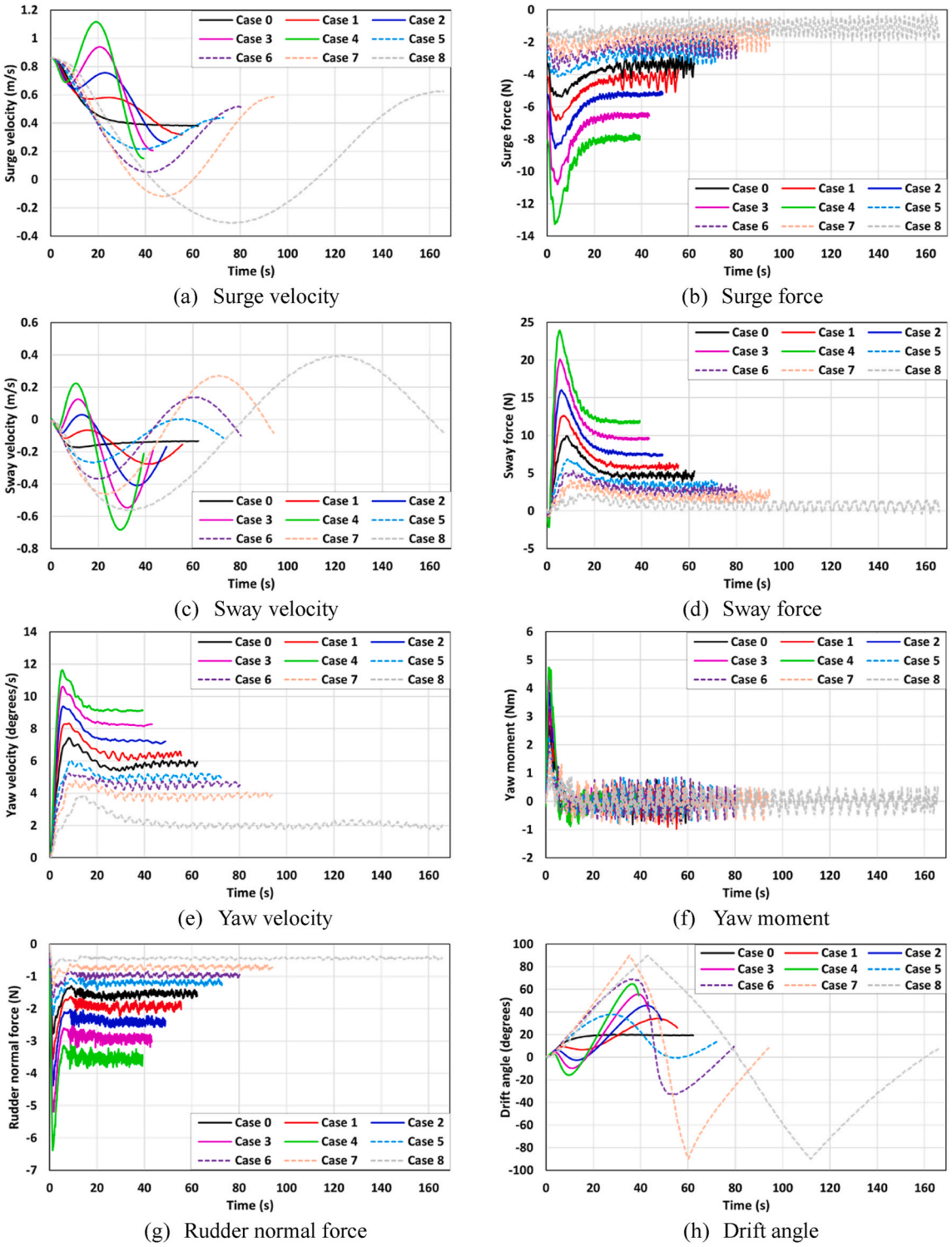


**Fig. 12.** The time histories of the ship velocities, forces and moments, and drift angles during the turning circle manoeuvre.

speed was attained.

The average values of the ship resistance and the propeller revolution rates at the self-propulsion condition are reported in Table 4. As can be seen, the presence of the current was found to result in noticeable changes in the ship resistance experienced by the advancing ship at self-propulsion when compared to Case 0 (the deep water without a current condition). For the ahead current conditions (Case 1–4), the increase of the current velocity led to a substantial increase in the ship resistance with consequent demand for the additional propulsion power to achieve the same approach speed. For the following current conditions (Case 5–8), on the other hand, the ship resistance was found to gradually decrease with the decrease in the current velocity. It has to be noticed that the propeller revolution rate to reach the same approaching speed was remarkably different from each case due to the different current contributions to the ship resistance. In this sub-section, the effects of currents on the ship motions at self-propulsion were not discussed since only small amplitudes of the ship motions (i.e., roll, heave, and pitch) were numerically observed, mainly due to the absence of incident waves

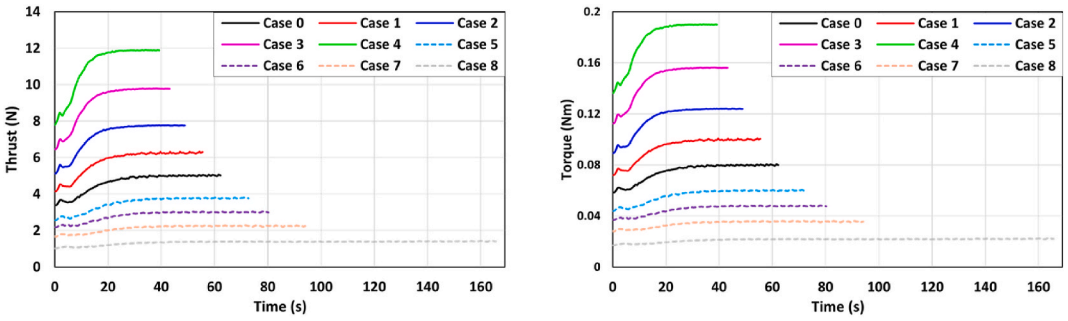


**Fig. 13.** The time histories of the propeller characteristics during the turning manoeuvre.

in this work.

A zoomed view of the instantaneous free surface elevation around the ship at self-propulsion is depicted in Fig. 10. The markedly different wave patterns around the KCS can be clearly seen from the figure, despite the same approaching speed (Fr = 0.157). This may be mainly attributed to the strong interaction between the Kelvin waves generated by the ship and the current. The effects of the different propeller revolution rates on the stern waves were also clearly shown, evidenced by the different free surface elevations at the stern region.

### 3.3. Turning circle manoeuvre

#### 3.3.1. Turning indices and time histories during the turning manoeuvre

This sub-section will provide the details of the numerical results for the free-running manoeuvres with particular emphasis on the turning performance of the ship operating in different currents (such as ahead and following current conditions). The contribution of different currents to the ship's turning behaviour was analysed in detail by comparison with its inherent behaviour in deep water without a current (Case 0). The results presented in this sub-section addressed the turning manoeuvres with only yaw angle variation up to 360° as implemented in the validation study. It is expected that the manoeuvring ship in the currents (Case 1–8) may experience substantial changes in the turning capability when compared to that observed in deep water without a current, attributed to the hydrodynamic effects caused by the presence of the current.

The ship trajectories predicted by the free-running CFD model performing the turning manoeuvre in accordance with the control mechanism (given by Eq. (14)) are displayed in Fig. 11, expressed with respect to the earth-fixed reference frame. In the figure, all the rudder activation points were shifted to the origin (0,0) of the reference frame for the sake of the correct comparisons of the ship paths. The turning indices for each case are also reported in Table 5, which can be determined from the obtained trajectories as defined in ITTC (2021a). It was evident that the inclusion of the current noticeably affects the ship trajectory and its turning parameters, clearly evidenced in the figure and table. The ship's heading angle continued to change while turning, leading to continual changes in the current-encounter direction during the manoeuvre. As a result, the acceleration and deceleration phenomena of the ship's speed occurred with the variation of the current-encounter direction. For example, a ship advancing in the ahead currents (Case 1–4) encountered the current from the bow direction (0° turn), from the port beam (90° turn), from the stern (180° turn), from the starboard beam (270° turn), and again from the bow (360° turn) in series after starting the starboard turning manoeuvre. The ship's velocity was decelerated by the ahead currents (from the bow) or accelerated by the following currents (from the stern) during the manoeuvre, consequently leading to substantial changes in the turning behaviour of the ship. It is confirmed that the presence of the current caused the drift of the path towards the current propagation direction, such that the turning trajectories were significantly deformed under stronger current conditions when compared to Case 0. When the ship was manoeuvring in the ahead current conditions (Case 1–4), it was revealed that the greater current velocity led to the smaller ship advance. On the contrary, the ship showed an opposite tendency in the following current conditions (Case 5–8). Unlike the remarkable changes in the advance, the ship experienced a slight change in the transfer and tactical diameter for both the ahead and following current conditions. Different propeller revolution rates applied to the CFD model (to obtain the same approach speed at a given condition) resulted in noticeable differences in the time taken for the 90°/180° turn. The greater propeller thrust led to the shorter 90°/180° turning time, generating the larger rudder normal force when the rudder blade was deflected. It seems difficult to sufficiently characterise the trajectories experienced by the ship operating in strong currents by means of the turning indices, as can be inferred from Fig. 11 and Table 5.

The time histories of the velocities, forces and moments, and drift angles experienced by the ship during the turning manoeuvre were displayed in Fig. 12, where each case is indicated with a different colour. It was observed for all cases that the ship started to turn towards the starboard side immediately after the execution of the rudder due to the increased rudder normal force (Fig. 12 (g)). After the rudder completed its deflection (35°), the ship experienced the peak value for the rudder normal force. The ship operating in the ahead currents (Case 1–4) led to a larger rudder normal force peak (mainly attributed to the relatively large propeller revolution rate) than the following current conditions (Case 5–8), consequently, caused larger yaw moment and yaw velocity peaks (Fig. 12 (e) and (f)). Then, the rudder normal force exhibited a gradual decrease (because of the decrease in the mean effective angle of attack of the rudder) and finally stabilised. The trends observed for the yaw velocity and yaw moment were similar to the behaviour of the rudder force. From Fig. 12 (a) and (c), it clearly appeared that the differences were remarkable in terms of the surge and sway velocities experienced by the ship in the currents (Case 1–8), characterised by the acceleration and deceleration phenomena due to the current. Such perceptible differences in the surge and sway velocities are the main contributions to the differences in the predicted ship trajectories, as evidenced in Fig. 11. The surge and sway velocities finally converged to a steady value for Case 0, whereas they showed a changing trend that continued to decrease and increase during the turn for Case 1–8 (stemming from the presence of the current). In this regard, the drift angle $\beta^{'}$ experienced by the ship in the currents (Case 1–8) also followed a similar trend, showing continuous changes in the drift angle during the manoeuvre (the drift angle $\beta^{'}$ is expressed by $\sin\beta^{'} = -\frac{Sway\ velocity}{Absolute\ velocity}$) (Fig. 12 (h)).

In Fig. 13, the different characteristics of the propeller in the currents during the turning manoeuvre can be appreciated in terms of the thrust and torque. A larger increase in the thrust was observed after the rudder deflection for the ahead currents (Case 1–4), whereas a relatively small increase was noted for the following currents (Case 4–8). The behaviour

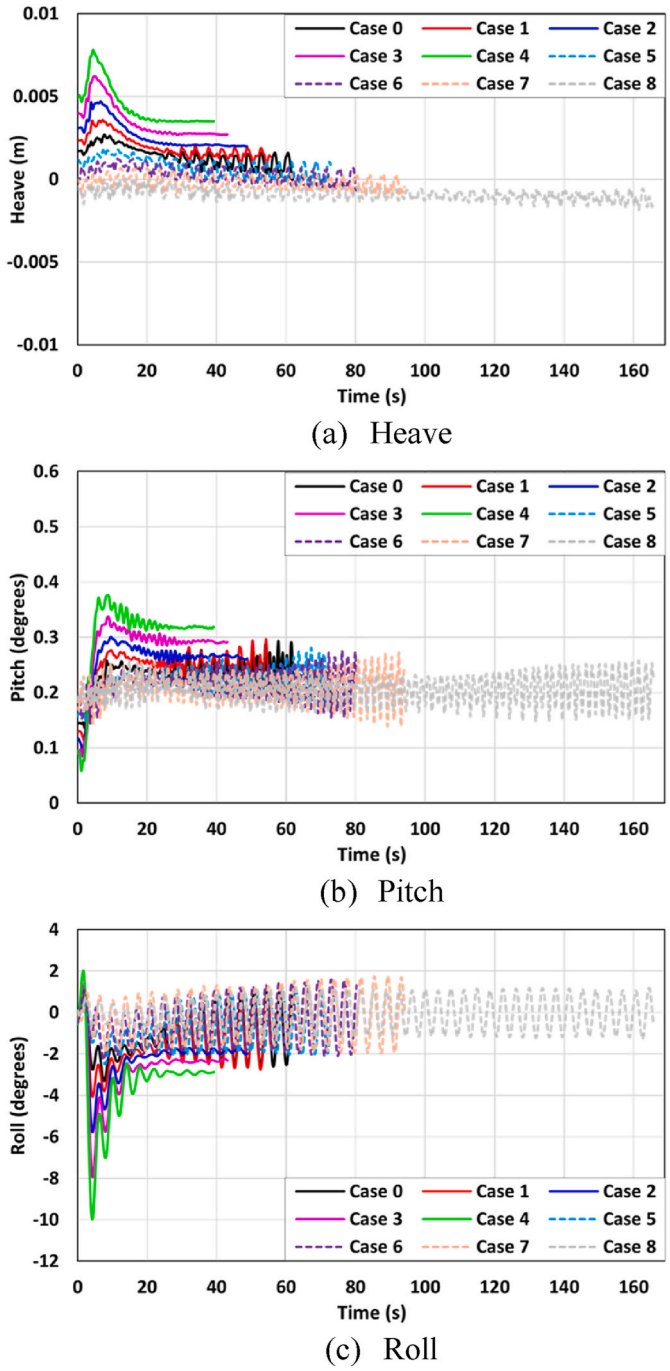


**Fig. 14.** The time histories of the ship motions during the turning manoeuvre.

of the torque was similar to the thrust. As mentioned previously, the volume-averaged velocity over the inflow velocity plane was an important factor in the determination of the performance of the propeller, which was dependent on the complicated interaction between the propeller revolution rate, the presence of the current, and the propeller wake velocity field.

Fig. 14 shows the time histories of the heave, pitch, and roll motions during the turning manoeuvres. A rapid increase in the pitch and heave displacements was observed during the beginning of the turn, and, after a peak, they converged to a certain value after approximately two-quarters of the turn. The self-propelled ship performing the turning manoeuvre can be characterised by the trim by stern condition (the condition in which a vessel inclines aft). The ship operating in the ahead currents (Case 1–4) experienced a relatively large roll angle during the manoeuvre, attributed to the strong lateral force acting on the rudder (related to the initial peak roll angle) and the hydrodynamic forces and the centrifugal force acting on the hull (associated with the second peak). The ship with the maximum propeller rate exhibited the maximum roll angle of 10° (i.e., under the maximum velocity of the current condition, Case 4). Relatively small roll angles of less than two degrees were observed for the following current conditions (Case 5–8).

Understanding the speed through water (STW) experienced by a manoeuvring ship in navigation practice is critical for making proper decisions on collision avoidance. STW is the speed of the vessel relative to the water, which is required to be used in ARPA (automatic radar plotting aids) radars to provide an accurate estimate of the target's aspect (for radar collision avoidance). It is worth noting that Fig. 12 (a) and (b) represent the speed over ground (SOG) which is the speed of the vessel relative to the surface of the earth (closely associated with the trajectory experienced by the ship). Fig. 15 presents the time histories of the ship surge and sway velocities with respect to STW during the turning manoeuvres. The differences were remarkable between the speeds over ground (Fig. 12 (a) and (b)) and the speeds through water (Fig. 15 (a) and (b)), demonstrating that currents are the main factor responsible for the difference between SOG and STW. It was observed that all the speeds through water showed a similar trend to the speeds experienced by the ship in deep water without a current. STW is totally consistent with SOG when the ship operates in water without a current (for example, Case 0). The speeds through water were noted to be relatively large when the ship was performing the turning manoeuvre at the relatively large propeller revolution rate.

### 3.3.2. *Corrected trajectories*

IMO (2002) states that the turning trajectory of a ship in calm water (i.e., the inherent turning capability) can be obtained by the correction for the drift effect of external disturbances on the ship's turning trajectory measured in currents, winds, and waves. As the present study only considered the current effects on the ship's manoeuvrability, the attention was devoted to the correction for the drift effect of currents on the trajectory in this sub-section. According to the guidelines of IMO (2002), the ship's trajectory, the heading angle, and the elapsed time should be recorded at least until the ship's heading variation reaches 720° to determine the local surface current velocity experienced by the ship. Based on this, additional computations were performed for Cases 1, 2, 5, and 6 (which were selected as representative cases to present the corrected trajectory) until a 720° change of heading angle was achieved. The obtained results after the ship's heading variation of 180° were used to estimate the magnitude and direction of the current in the assumption that the yaw velocity is steady after 180° turn. Positions $(x_{1i}, y_{1i}, t_{1i})$ and $(x_{2i}, y_{2i}, t_{2i})$ in Fig. 16 indicate the positions of the ship which have a phase difference of 360°. The local current velocity $\boldsymbol{V}_i$ for any two corresponding positions is defined as the follows:

$$\boldsymbol{V}_i = \frac{(x_{2i} - x_{1i},\quad y_{2i} - y_{1i})}{(t_{2i} - t_{1i})} \tag{15}$$

The estimated mean current velocity can be obtained from the following equation:

$$\boldsymbol{V}_e = \frac{1}{n}\sum_{i=1}^{n} \boldsymbol{V}_i = \frac{1}{n}\sum_{i=1}^{n} \frac{(x_{2i} - x_{1i},\quad y_{2i} - y_{1i})}{(t_{2i} - t_{1i})} \tag{16}$$

The obtained trajectories in the currents can be corrected as follows:

$$\boldsymbol{X}'(t) = \boldsymbol{X}(t) - \boldsymbol{V}_e t \tag{17}$$

in which $\boldsymbol{X}(t)$ is the measured position vector and $\boldsymbol{X}'(t)$ is the corrected trajectory of the ship ($\boldsymbol{X}'(t) = \boldsymbol{X}(t)$ at $t = 0$).

The corrected trajectories (for Case 1, 2, 5, and 6) calculated by the above equations are depicted in Fig. 17. In the figure, the uncorrected results (indicated with red colour) and the inherent turning trajectory (Case 0, black line) are also presented for comparison purposes. As can

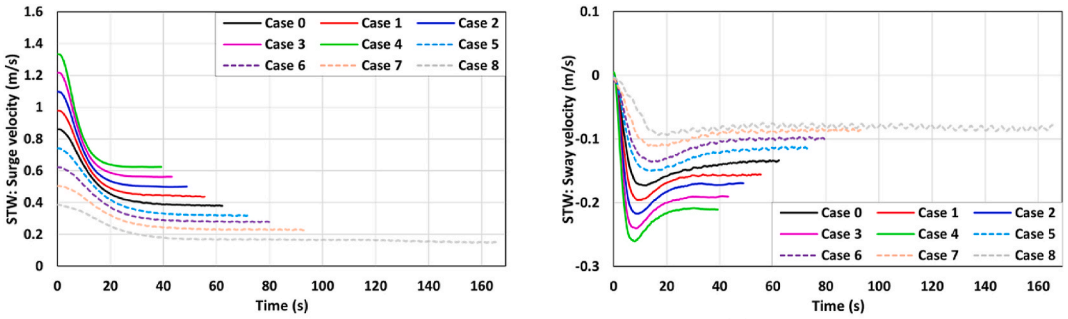


(a) STW: Surge velocity (b) STW: Sway velocity

**Fig. 15.** The time histories of the ship velocities with respect to the speed through water (STW) during the turning manoeuvre.

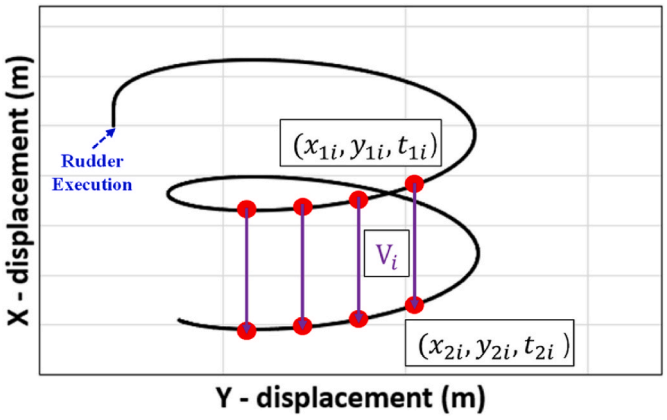


**Fig. 16.** Turning trajectory in a current.

be seen from the figure, some discrepancies between the corrected trajectories and Case 0 were observed for all cases. The possible reason for such discrepancies may be related to the non-uniformity of $V_i$ caused by the assumption that yaw rate is stabilised. It is confirmed that the discrepancies are much more pronounced in stronger currents. This implies that the accurate estimation of the inherent turning trajectory is challenging, especially when using the results measured in strong currents to calculate the corrected trajectory.

## 4. Conclusions and discussion

In this work free-running CFD simulations to predict the turning capability of a container ship (the KCS model) in different current conditions have been carried out, along with comparisons with the inherent ship manoeuvrability in deep water without a current. All analyses have been performed by means of the commercial CFD code STAR-CCM+.

Firstly, a numerical scheme for the CFD model capable of performing a self-propelled free manoeuvre was proposed to carry out such manoeuvring analyses in different currents. The detailed procedures of the numerical approach regarding propeller modelling, mesh generation, time step selection, and boundary conditions were illustrated in detail in this paper.

Next, a validation study was carried out to assess the validity of the CFD model by comparison with the available experimental results from a free-running test. In turning indices predictions, it was revealed that the present CFD model predicted the ship advance, transfer, and tactical diameter with a range of 0.97–3.72% of the EFD data. In addition, the CFD results for the kinematic parameters, ship motions, and propeller parameters during the manoeuvre were found in good agreement with the experiment. The acceptable agreement between CFD and EFD demonstrated the reliability of the current CFD model when dealing with manoeuvring problems.

Following this, a series of turning manoeuvres (eight simulation cases) in deep waters with current speed to ship speed ratios varying between −0.552 and −0.138/+0.138 and + 0.552 were carried out using the present CFD model. The results were combined and plotted in form of graphs in order to enable the current effect on the ship manoeuvrability to be presented clearly. The main results drawn from this study can be summarised as follows:

1) It was found that the presence of the current resulted in noticeable changes in the resistance experienced by the advancing ship to achieve the self-propulsion condition when compared to that in deep water without a current. When it comes to the ahead current conditions, as expected, the increase of the current velocity caused a substantial increase in the ship resistance with consequent demand for the additional propulsion power to reach the same approach speed (Fr = 0.157). For the following current conditions, on the contrary, the ship resistance exhibited a gradual decrease with the decrease in the current velocity.
2) It can be concluded that the inclusion of the current has a remarkable influence on the turning performance of the ship, leading to significant changes in the ship trajectory and its turning parameters (compared to the inherent ship manoeuvrability, Case 0). When the ship started the standard turning manoeuvre in the ahead currents (Case 1–4), the ship advance became remarkably smaller with an increase in the current velocity. On the other hand, in the following currents (Case 5–8), a larger increase was observed in the advance as the current velocity increased. Unlike the marked changes in the ship advance, slight changes in the transfer and tactical diameter for both ahead and following currents were observed.
3) It was revealed that the differences were remarkable in terms of the surge and sway velocities experienced by the manoeuvring ship in the currents (Case 1–8), characterised by the acceleration and deceleration phenomena due to the current. Given that the ship's velocities in the horizontal plane may be decisive for the ship trajectory and its parameters, such perceptible differences in the surge and sway velocities can be considered as the main contributions to the differences in the predicted ship trajectories. It was observed that only small heave and pitch displacements occurred during the manoeuvre for all cases. The ship experienced a relatively large roll motion (up to 10°) when starting the turn in the ahead currents, whereas a small roll motion of less than two degrees was observed for the following currents.

A ship's turn plays an important role in navigational safety at sea. Such a turning behaviour, occurring in response to the rudder deflection, can be implemented for the purpose of a course alteration based on voyage plans or collision avoidance to prevent a close-quarters situation. It should be borne in mind that the manoeuvring performance of a ship (for example, the turning capability) differs depending on the presence

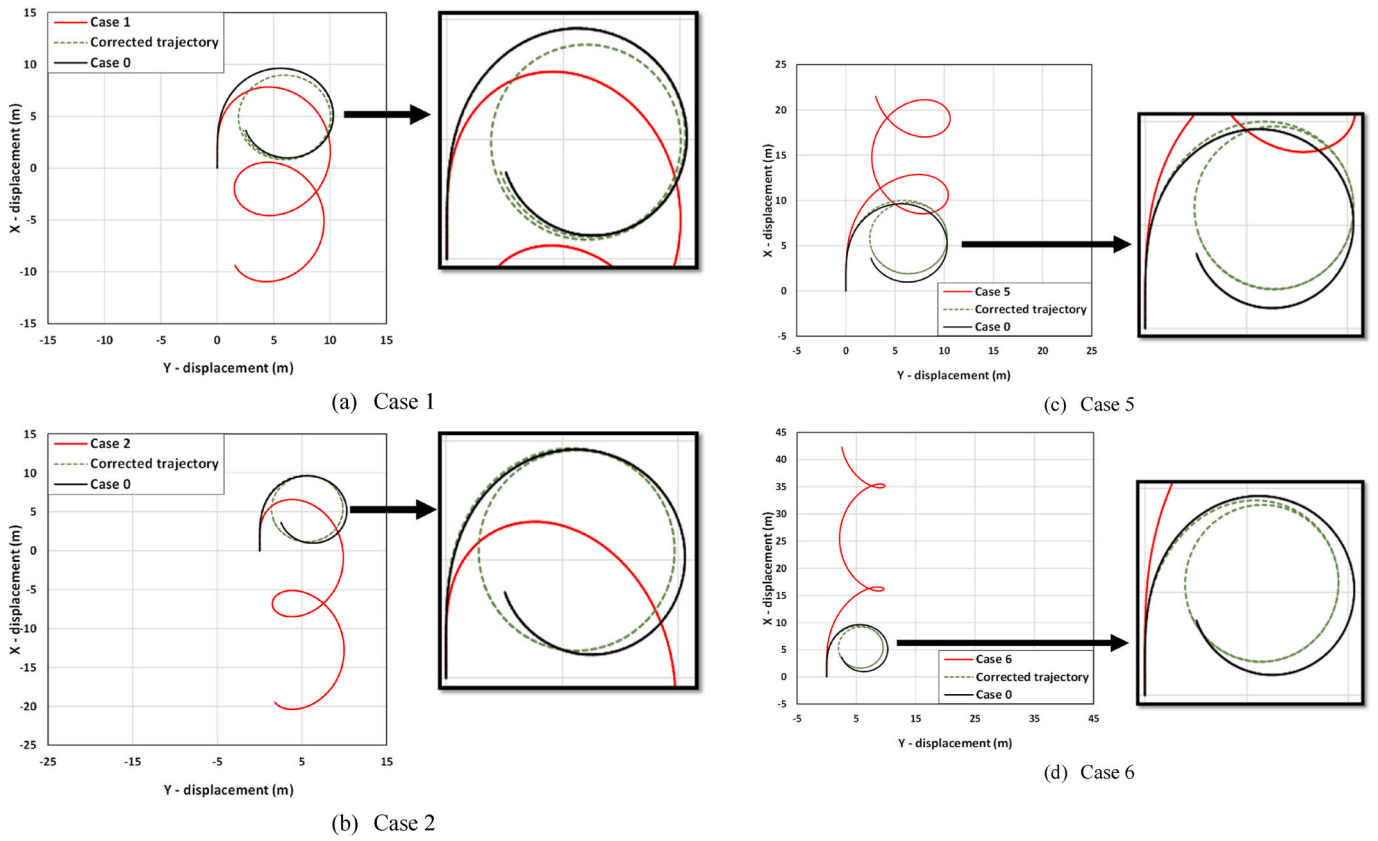


**Fig. 17.** The corrected trajectories for Cases 1, 2, 5, and 6.

of external disturbances such as winds, waves, and currents. Thus, Master Mariners and navigating officers, who are responsible for ship handling actions, should fully understand a ship's manoeuvrability under a given environmental condition for safe ship operation. Unfortunately, they can only access the information regarding turning and zigzag manoeuvres in calm water, generally measured from full-scale sea trials or model-scale experiments in accordance with the recommendation by IMO (2002). In this regard, it is believed that this study could provide a practical insight into the turning performance of commercial vessels in different currents (regarded as one of the dominant environmental loads), contributing to enhancing navigational safety at sea.

This paper has furnished a very useful starting point for investigations into ship manoeuvrability in a current by means of URANS simulations. This research could further add values by taking into account the presence of waves and winds together with currents, as these will also have a remarkable influence on the manoeuvring behaviour of a ship. Using the methodology presented in Kim et al. (2021c), further studies into ship manoeuvrability in waves with currents could be made. The study should also be extended to investigate the manoeuvrability of the ship with the same propeller rate (i.e., the same speed through water) under different current conditions such as a combination of various current speeds and directions.

## CRediT authorship contribution statement

**Daejeong Kim:** Writing – original draft, Conceptualization, Methodology, Formal analysis, Investigation, Validation, Visualization, Data curation. **Tahsin Tezdogan:** Conceptualization, Methodology, Supervision, Writing – review & editing, Resources, Supervision. **Atilla Incecik:** Supervision, Writing – review & editing, Resources, Supervision.

## Declaration of competing interest

The authors declare that they have no known competing financial interests or personal relationships that could have appeared to influence the work reported in this paper.

## Acknowledgements

It should be noted that the results were obtained using the ARCHIE-WeSt High Performance Computer (www.archie-west.ac.uk) based at the University of Strathclyde.

## References

Abkowitz, M.A., 1964. Lectures on Ship Hydrodynamics–Steering and Manoeuvrability.
Broglia, R., Dubbioso, G., Durante, D., Di Mascio, A., 2013. Simulation of turning circle by CFD: analysis of different propeller models and their effect on manoeuvring prediction. Appl. Ocean Res. 39, 1–10.
Broglia, R., Dubbioso, G., Durante, D., Di Mascio, A., 2015. Turning ability analysis of a fully appended twin screw vessel by CFD. Part I: single rudder configuration. Ocean Eng. 105, 275–286.
Carrica, P.M., Mofidi, A., Eloot, K., Delefortrie, G., 2016. Direct simulation and experimental study of zigzag maneuver of KCS in shallow water. Ocean Eng. 112, 117–133.
Demirel, Y.K., Turan, O., Incecik, A., 2017. Predicting the effect of biofouling on ship resistance using CFD. Appl. Ocean Res. 62, 100–118.
Di Mascio, A., Broglia, R., Muscari, R., 2007. On the application of the single-phase level set method to naval hydrodynamic flows. Comput. Fluid. 36 (5), 868–886.
Dubbioso, G., Durante, D., Di Mascio, A., Broglia, R., 2016. Turning ability analysis of a fully appended twin screw vessel by CFD. Part II: single vs. twin rudder configuration. Ocean Eng. 117, 259–271.
Hasanvand, A., Hajivand, A., 2019. Investigating the effect of rudder profile on 6DOF ship turning performance. Appl. Ocean Res. 92, 101918.
Hasanvand, A., Hajivand, A., Ali, N.A., 2021. Investigating the effect of rudder profile on 6DOF ship course-changing performance. Appl. Ocean Res. 117, 102944.
IMO, 2002. Explanatory Notes to the Standards for Ship Manoeuvrability.
IMO, 2014. 2013 Interim Guidelines for Determining Minimum Propulsion Power to Maintain the Manoeuvrability of Ships in Adverse Conditions.

Inoue, S., Hirano, M., Kijima, K., Takashina, J., 1981. A practical calculation method of ship maneuvering motion. Int. Shipbuild. Prog. 28 (325), 207–222.
ITTC, 2014. ITTC - Recommended Procedures and Guidelines : Practical Guidelines for Ship CFD Applications.
ITTC, 2017. Tasks and Structure of 29th ITTC Technical Committees and Groups. version 4.
ITTC, 2021a. ITTC - Recommended Procedures and Guidelines: Full Scale Manoeuvring Trials.
ITTC, 2021b. The Manoeuvring Committee Final Report and Recommendations to the 29th ITTC.
Kavli, H.P., Oguz, E., Tezdogan, T., 2017. A comparative study on the design of an environmentally friendly RoPax ferry using CFD. Ocean Eng. 137, 22–37.
Kim, D., Song, S., Jeong, B., Tezdogan, T., 2021a. Numerical evaluation of a ship's manoeuvrability and course keeping control under various wave conditions using CFD. Ocean Eng. 237, 109615.
Kim, D., Song, S., Jeong, B., Tezdogan, T., Incecik, A., 2021b. Unsteady RANS CFD simulations of ship manoeuvrability and course keeping control under various wave height conditions. Appl. Ocean Res. 117, 102940.
Kim, D., Song, S., Sant, T., Demirel, Y.K., Tezdogan, T., 2022a. Nonlinear URANS model for evaluating course keeping and turning capabilities of a vessel with propulsion system failure in waves. Int. J. Nav. Archit. Ocean Eng. 14, 100425.
Kim, D., Song, S., Tezdogan, T., 2021c. Free running CFD simulations to investigate ship manoeuvrability in waves. Ocean Eng. 236, 109567.
Kim, D., Tezdogan, T., 2022. CFD-based hydrodynamic analyses of ship course keeping control and turning performance in irregular waves. Ocean Eng. 248, 110808.
Kim, D., Tezdogan, T., Incecik, A., 2022b. Hydrodynamic analysis of ship manoeuvrability in shallow water using high-fidelity URANS computations. Appl. Ocean Res. 123, 103176.
Kim, I.-T., Kim, C., Kim, S.-H., Ko, D., Moon, S.-H., Park, H., Kwon, J., Jin, B., 2021d. Estimation of the manoeuvrability of the KVLCC2 in calm water using free running simulation based on CFD. Int. J. Nav. Archit. Ocean Eng.
Liu, C., Wang, J., Wan, D., 2020. CFD simulations of self-propulsion and turning circle maneuver up to 90° of ship in waves. J. Ship Res. 1–14.
Menter, F.R., 1994. Two-equation eddy-viscosity turbulence models for engineering applications. AIAA J. 32 (8), 1598–1605.
Mofidi, A., Carrica, P.M., 2014. Simulations of zigzag maneuvers for a container ship with direct moving rudder and propeller. Comput. Fluid. 96, 191–203.
Perić, R., Abdel-Maksoud, M., 2018. Analytical prediction of reflection coefficients for wave absorbing layers in flow simulations of regular free-surface waves. Ocean Eng. 147, 132–147.
Shen, Z., Wan, D., Carrica, P.M., 2015. Dynamic overset grids in OpenFOAM with application to KCS self-propulsion and maneuvering. Ocean Eng. 108, 287–306.
Siemens, 2020. Simcenter STAR-CCM+ Documentation.
SIMMAN, 2020. Workshop on Verification and Validation of Ship Manoeuvring Simulation Methods.
Terziev, M., Tezdogan, T., Incecik, A., 2019. A geosim analysis of ship resistance decomposition and scale effects with the aid of CFD. Appl. Ocean Res. 92, 101930.
Terziev, M., Tezdogan, T., Incecik, A., 2020. Application of eddy-viscosity turbulence models to problems in ship hydrodynamics. Ships Offshore Struct. 15 (5), 511–534.
Tezdogan, T., Demirel, Y.K., Kellett, P., Khorasanchi, M., Incecik, A., Turan, O., 2015. Full-scale unsteady RANS CFD simulations of ship behaviour and performance in head seas due to slow steaming. Ocean Eng. 97, 186–206.
Tezdogan, T., Incecik, A., Turan, O., 2016. Full-scale unsteady RANS simulations of vertical ship motions in shallow water. Ocean Eng. 123, 131–145.
Wang, J., Wan, D., 2018. CFD investigations of ship maneuvering in waves using naoe-FOAM-SJTU Solver. J. Mar. Sci. Appl. 17 (3), 443–458.
Wang, J., Zhao, W., Wan, D., 2016. Self-propulsion Simulation of ONR Tumblehome Using Dynamic Overset Grid Method. Shanghai Jiao Tong Univ. Collaborative Innovation Center for Advanced Ship and Deep-Sea Exploration, USA.
Wang, J., Zou, L., Wan, D., 2017. CFD simulations of free running ship under course keeping control. Ocean Eng. 141, 450–464.
Wang, J., Zou, L., Wan, D., 2018. Numerical simulations of zigzag maneuver of free running ship in waves by RANS-Overset grid method. Ocean Eng. 162, 55–79.
Yasukawa, H., Yoshimura, Y., 2015. Introduction of MMG standard method for ship maneuvering predictions. J. Mar. Sci. Technol. 20 (1), 37–52.